2016 IEEE GRSS STRATUS Workshop

Systems and Technologies for Remote Sensing Applications Through Unmanned Aerial Systems

28 October 2016

Louise Slaughter Hall
Rochester Institute of Technology
Rochester, New York, USA

STRATUS 2016
28 October 2016
Louise Slaughter Hall, Rochester Institute of Technology
Agenda

Time	Topic	Speaker
0800-0830	Registration/Breakfast	
0830-0900	Welcome by STRATUS Chair, RIT VP of Research on UAS Signature Program, and Technical Program Chair	Emmett Ientilucci, RIT Ryne Raffaelle, RIT John Kerekes, RIT
0900-0935	**Keynote 1**: Integrating UAVs with Sensing Instruments: Challenges and Opportunities	Peter Clemens, Headwall
0935-1010	**Keynote 2**: UAS Signature Research Program	David Messinger, RIT
1010-1030	Early Lessons from UAS Case Law	Josephine Wolff, RIT
1030-1050	**Coffee Break**	
1050-1110	Eye-tracking Drone Pilots View During First Person View (FPV) Flight	Jason Babcock, Positive Science
1110-1130	Increased Automation of Flight Planning for Small UAS Conducting Imaging Tasks	Paul Sponagle, RIT
1130-1150	Quadrotor Controller Development via Model Based Design	Daniel Kaputa, RIT
1150-1210	Quantification of Cyanobacteria Blooms Using UAS Imagery	Ryan Ford, RIT
1210-1400	**Lunch and Poster Presentations**	
1400-1420	Small Unmanned Aircraft Systems (sUAS or drone) Technology is Transforming the Face of Business.	Brian Pitre, SkyOp
1420-1440	Miniaturized VNIR-SWIR Hyperspectral Sensor Technology Platform for Unmanned Aerial Systems	Sam Hill, Headwall
1500-1520	Design of an Integrated Propane Fuel Reformer and Fuel Cell System for Unmanned Aerial System (UAS) Applications	Michael Waller, RIT
1440-1500	Ultra Thin Solar Cell Used in UAVs Employing Surface Plasmon Polariton (SPP)	Richard Kyung, CRG
1520-1540	**Coffee Break**	
1540-1550	**Student Prize Presentation**	
1550-1650	Panel Discussion Panelists: Peter Clemens, David Messinger, Brian Pitre, Josephine Wolff Moderator: John Kerekes	
1650-1700	Closing Remarks	Emmett Ientilucci, RIT

Poster	Title	Author
1	Use of a UAV for Water Sampling to Assist Remote Sensing of Bacterial Flora in Freshwater Environments	Fernando Ontiveros, St. John Fisher
2	System Modeling and Identification of Unmanned Quad Rotor Air Vehicle based on subspace and PEM	Yi Liu, Beijing Institute of Technology
3	Benewake's LiDAR Products Introduction	York Chen, Benewake
4	A Simple and Effective Semi-supervised Learning Framework for Hyperspectral Image Classification	Ahmed Elshamli, University of Guelph
5	Detecting White Mold Onset in Snap Beans Using Spectral Remote Sensing With and Extension to Unmanned Aerial Systems (UAS)	Sadie Wolters, RIT
6	On Mapping Corn Yield Using Structure-from-motion Data from Unmanned Aerial Systems	Seth Baker, RIT

Welcome from Workshop Chair

On behalf of the organizing committee, we would like to welcome everyone to the 1st workshop on Systems and Technologies for Remote Sensing Applications Through Unmanned Aerial Systems (STRATUS 2016). The one-day workshop is being held in Rochester, New York, on October 28, 2016 at the Rochester Institute of Technology (RIT) home to some 18,000 students.

The workshop was made possible, in part, by an IEEE Geoscience and Remote Sensing Society (GRSS) local chapter award. This award, along with the generous sponsorship of Pictometry, an EagleView Company, allowed us to keep registration fees low while waiving said fees for students. The workshop also received the technical co-sponsorship of the IEEE GRSS enabling us to host the event on the IEEE GRSS website and advertise in the GRSS Magazine, and publish the accepted full papers on IEEE Xplore.

The aim of the workshop is to facilitate interaction between academic researchers, industry researchers and students working in the field of remote sensing utilizing unmanned aerial systems. Since this is an emerging field, the goal of the workshop is not to *define* technical requirements, standards or legal policy, but rather to illustrate the specific connection between remote sensing and unmanned aerial platforms at both the commercial and academic levels. We aim to bring together academics, industry representatives, and domain specialists to share perspectives on this rapidly evolving topic.

This first workshop consisted of two submission options; 1) a four-page peer-reviewed publication (plus presentation/poster) or 2) an abstract of recent research (plus presentation/poster). We received a total of 11 abstracts and four full papers to include in this proceeding resulting in nine presentations and six posters. The two keynote speakers are from industry and academia and will shed light on the integration of UAV's with sensing instruments and RIT's new UAS Signature Research Program. The workshop concludes with a student award for best poster / presentation and a panel discussion consisting of individuals representing industry, academia, and case law.

We believe this program will promote the dissemination of research results and technical advances in this new emerging field of unmanned aerial systems. It is our intention that this be the start of an annual workshop on the subject. Lastly, we hope you enjoy the workshop and look forward to your participation.

Sincerely,

Dr. Emmett Ientilucci
STRATUS 2016 Workshop General Chair

Table of Contents

Keynote 1: Integrating UAVs with Sensing Instruments: Challenges and Opportunities

Peter Clemens, Headwall Photonics

Hyperspectral imaging is one of several highly precise 'remote sensing' technologies that have successfully evolved from the defense/ISR community. Headwall is a highly innovative and entrepreneurial manufacturing company located near Boston that has harnessed and refined this technology for use in a number of commercial applications.

This successful 'commercialization' effort is a byproduct of pairing spectroscopy and imaging to deliver a rich amount of spectral and spatial data in the ranges well beyond the visible. With this data, the scientific research community can see the early signs of diseases on crops from UAVs, uncover hidden features in cultural treasures, inspect food products with unmatched clarity and precision, and non-invasively detect the onset of degenerative diseases. Among the largest commercial application areas for hyperspectral imaging is 'remote sensing' from airborne platforms. Although satellites and fixed-wing aircraft have been used, UAVs are rapidly becoming the 'go-to' platform because of simplicity and affordability. This drives another evolutionary trend, as instrument payloads are getting smaller and lighter.

In this presentation we discuss the confluence of sensors and UAV technology, pinpoint why 'integrated airborne solutions' are preferred, unveil the basics behind hyperspectral imaging, and touch on the evolution of software as a catalyst for even more rapid adoption.

Keynote 2: UAS Imaging Signature Research Program at RIT

David Messinger, Rochester Institute of Technology

The recent emergence of low cost, small unmanned aerial systems (sUAS) coupled with increasingly capable micro-imaging sensors such as hyperspectral, multispectral, thermal infrared, and LiDAR is resulting in a virtual explosion of new decision support applications. We see multiple opportunities to integrate this technology to the benefit of several industrial sectors and are conducting research into systems, operations, and data processing workflows across a wide range of applications.

Nowhere is the benefit of these emergent capabilities more apparent and have higher impact than in the domains of precision agriculture, environmental monitoring, and infrastructure inspection. Incorporation of sUAS platforms has the potential to improve effectiveness, increase overall safety and decrease the time involved in performing field inspections and surveys.

Recognizing this enormous potential, RIT has made a major strategic investment in UAS-based imaging research. The effort is being led by the Digital Imaging and Remote Sensing (DIRS) laboratory within the Chester F. Carlson Center for Imaging Science with participation from the College of Engineering, College of Applied Science and Technology, and the College of Liberal Arts. The program conducts fundamental research that is the first step in developing automated image-based assessment systems for use in the key application areas.

This presentation will discuss this exciting new program at RIT, outlining the technology being used and showing early results from our first season of flying.

Early Lessons from UAS Case Law

Josephine Wolff, Rochester Institute of Technology

As courts are beginning to address legal issues related to the use of commercial and personal unmanned aerial systems (UAS), a small body of case law is emerging around how the courts deal with private property, safety, and privacy issues related to the use of these devices. This presentation will review some of the recent and ongoing legal charges and civil penalties related to the use of UAS by individuals. We will discuss the case of William Merideth, who shot down a UAS over his property in Kentucky, the FAA's actions against Raphael Pirker who piloted a UAS to capture video of the University of Virginia as part of an advertising shoot, as well as the ongoing investigation of Austin and Bret Haughwout who mounted weapons to a UAS. The presentation will focus on the implications of these incidents for UAS operators and commercial uses of the technology, as well as outlining some of the ongoing debates and undecided issues in this area of law.

Eye-tracking Drone Pilots View During First Person View (FPV) Flight

Jason Babcock, Positive Science, Gabriel Diaz, Rochester Institute of Technology, and Jeff Pelz, Rochester Institute of Technology

The rapid development of UAV technology has energized the sport of drone racing. Pilots fly in first-person view (FPV), which is wireless video transmitted from a UAV camera to a head mounted display. Although FPV is more natural than line-of-sight (LOS) flying, FPV pilots face limited situational awareness. How do race pilots perform complex maneuvers during rapid flight? How can we better teach novice pilots?

We aim to explore methodologies to analyze drone pilot performance by recording control adjustments, optic flow patterns, and eye movements. We present a system that captures a pilot's eye movements while flying a 200mm-class quadcopter in FPV. This novel configuration allows for a more complete study of pilot behavior. Beyond drone racing, eye-tracking a drone pilot's visual strategies may prove valuable in roof/property inspections, agricultural analysis, crime scene investigations, training in UAV surveillance, and the analysis of graphical interfaces in VR-style headgear.

Increased Automation of Flight Planning for Small UAS Conducting Imaging Tasks

Paul Sponagle, Rochester Institute of Technology

An explosion in the availability of unmanned platforms has provided operators with a simplified means to address many tasks, including the creation of 3D models from high-resolution imagery. These models are derived from point clouds created using structure-from-motion approaches available both in commercial and open source software suites. The quality of these point clouds and their derived 3D models can vary widely. The key factors that contribute to this variability in model quality are the collection approach and the utilization of these turn-key software solutions. This presentation describes efforts underway at the Rochester Institute of Technology's Chester F. Carlson Center for Imaging Science to develop, implement, and evaluate the efficacy of novel flight planning techniques that feeds directly into commercial flight planning software (e.g. UgCS). An emulator will demonstrate an atypical flight path and the resulting 3D model will be displayed.

Quadrotor Controller Development via Model Based Design

Daniel Kaputa, Rochester Institute of Technology

Low cost compute platforms such as the Raspberry PI and advances in 3D printing have changed the technical landscape for hobbyists, inventors, and engineers alike. These new tools provide the designer with a low cost method for performing rapid prototyping of embedded systems, however the daunting task of algorithm development still lurks in the shadows. Traditionally, programs are hand-coded in languages such as C or Python and there is an inherent disconnect between the deployed code and the high level system model. This disconnect between domains increases the likelihood of bugs creeping into the code. Model based design provides a way to accelerate algorithm development and minimize coding errors by placing the system model at the center of the development process from requirements though design, implementation, and testing. We present the development of a model based quadrotor controller created via the Simulink Coder product from the Mathworks.

Quantification of Cyanobacteria Blooms Using UAS Imagery

Ryan Ford, Rochester Institute of Technology, and Anthony Vodacek, Rochester Institute of Technology

Water monitoring authorities have become concerned with detecting and monitoring the increasing number of Cyanobacteria blooms in the Western New York region. Traditional airborne imaging systems are costly to fly, while satellite imaging systems generally have spatial resolutions too coarse for smaller waterbodies. Unmanned Aerial Systems (UAS) are not restrained by these limitations. A six band Tetracam camera array on a UAS collected imagery of the Honeoye Lake bloom on September 12, 2016. Water samples were collected simultaneously and analyzed for concentration of chlorophyll-a and phycocyanin, indicator pigments of cyanobacteria blooms. Concentrations of these pigments were retrieved from the imagery using a model based look-up-table (LUT) technique. LUTs were generated using the Hydrolight modeling software. The imagery was compensated for atmospheric effects by using an empirical line correction, and each pixel was compared to the LUT to find the best fitting spectra and their related concentrations. Further interpolation and minimization were then used to determine concentrations that fall between LUT entries. The concentrations retrieved from the imagery were compared to water samples to determine the retrieval accuracy. The results indicate potential for monitoring blooms in small water bodies using UAS imaging.

Small Unmanned Aircraft Systems (sUAS or drone) Technology is Transforming the Face of Business

Brian Pitre, SkyOp

Small Unmanned Aircraft Systems (sUAS or drone) technology is transforming the face of business. Once limited to military applications, growth in the American sUAS industry is shifting to commercial innovation, fundamentally changing the workplace and creating new jobs. The economic impact of drones over the next 10 years is estimated at $82 billion in the US alone, and drone units already outnumber manned aircraft. As it redefines efficiency and rewrites industry methodologies, drone technology will also give rise to new and unprecedented business models.

SUAS - JUST A FEW APPLICATIONS

A brief overview of application areas and post-processing.

- Agriculture
- Construction
- Inspection
- Insurance
- Land Surveyors
- Media & Marketing
- Media & Marketing
- Real Estate

POST-PROCESSING

- Mosaicing
- Infrared
- 3D Models
- Point Cloud

JUST RELAESED FAA REGULATIONS MAKE COMMERCIAL USE OF SMALL UNMANNED AIRCRAFT SYSTEMS THE HOTTEST NEW BUSINESS TECHNOLOGY

We'll cover how to prepare students for the FAA Operator's Certificate exam; it also includes the different types of flight systems and their capabilities, safe and legal flying practices, market opportunities and applications as well as piloting skills.

- 14 CFR Part 107 a 624-page document
- Released June 21, 2016
- Effective August 29, 2016
- Pass a written knowledge test
- General Aviation Knowledge Test
- 60 multiple-choice questions out of pool of 300
- A passing grade is 70%
- Receive a Remote pilot in Command Certification

- Schedule an appointment at a FAA Knowledge Center – FAA.gov
- Show ID, Date of Birth, Photo, Address, Signature, Cost $150
- Pass Test
- Airman Knowledge Test Report (AKTR)
- Apply for Airman Certificate
- Temporary approximately 10 days
- Permanent Certificate after vetted by TSA
  - o Up to 120 days
  - o Receive in mail
- Retesting every 24 months thereafter

The test knowledge areas are as follows:

1. Applicable regulations relating to small unmanned aircraft system rating privileges, limitations, and flight operation;
2. Airspace classification, operating requirements, and flight restrictions affecting small
3. Unmanned aircraft operation; Aviation weather sources and effects of weather on small unmanned aircraft performance;
4. Small unmanned aircraft loading;
5. Emergency procedures;
6. Crew resource management;
7. Radio communication procedures;
8. Determining the performance of small unmanned aircraft;
9. Physiological effects of drugs and alcohol;
10. Aeronautical decision-making and judgment;
11. Airport operations; and
12. Maintenance and preflight inspection procedures

WORKFORCE IMPACT OF FAA REGULATIONS

The news is filled with stories of risky, unchecked drone piloting. This happens because many drone operators are self-trained and unaware of best practices for piloting. New FAA regulations pave the way for expanded commercial use of drones. More importantly, they include a requirement that pilots pass a certification test in order to use a drone for commercial purposes. Before taking advantage of new employment opportunities, even the most experienced drone operators will need comprehensive instruction that includes the latest FAA regulations. Community colleges are uniquely positioned to deliver the knowledge and experience that hobbyists, job seekers, and business owners will need to pass the FAA's rigorous certification test.

THE SKYOP CURRICULUM: A COMMUNITY COLLEGE INNOVATION OPPORTUNITY

SkyOp presents a revenue-sharing educational opportunity for community colleges to capitalize on the economic wave being created by drones.

With SkyOp's Introduction to small Unmanned Aircraft Systems course, you can…

- Offer a nationally recognized, comprehensive drone-training program – quickly & profitably.
- Empower your local workforce to obtain licensure & access emerging job opportunities.
- Provide hobbyists with best safety practices and piloting skills.
- Access educator training, FAA updates & turnkey course marketing. By partnering with SkyOp, your school can connect your workforce to his new realm of employment opportunity.

THE FUTURE OF SUAS

There will be roughly 600,000 commercial drones taking to the air within the next year, according to the FAA. Transportation secretary Anthony Foxx says we are in "one of the most dramatic periods of change in the history of transportation," and thanks to a new regulation that makes it easier to become a commercial drone operator, the number is expected to increase 30-fold.

Miniaturized VNIR-SWIR Hyperspectral Sensor Technology Platform for Unmanned Aerial Systems

Sam Hill, Headwall Photonics, and Peter Clemens, Headwall Photonics

Modeling of carbon uptake-release requires knowledge about the quantity and type of vegetation at a location. Current models are limited by coarsely defined vegetation maps (PFTs). One method to improve PFTs is utilizing UAS and Hyperspectral Sensor Technology (HST) to discern between vegetative species on a fine scale. The problem with this concept is that HST Systems have not scaled in size with UAS and thus it has been difficult to attach HST to UAS with restricted SWaP demands. To address this problem Headwall Photonics (HPI) developed the "Ultra-HST", a full-spectrum (350nm-2500nm) miniaturized HST with embedded computation to collect and process data in real time from two co-aligned sensors. The Ultra-HST fits on UAS payloads of less than 5-lbs. while maintaining the spatial and spectral resolution of legacy remote-sensing HST Systems. HPI will review the current characterization of the Ultra-HST in the lab and in airborne field trials as well as discuss future improvements.

Design of an integrated propane fuel reformer and fuel cell system for unmanned aerial system (UAS) applications

Michael G. Waller, Mark R. Walluk and Thomas A. Trabold
Golisano Institute for Sustainability, Rochester Institute of Technology, Rochester, NY 14623
mgw7167@rit.edu / mrwasp@rit.edu / tatasp@rit.edu

***Abstract* — Recent fuel cell research has focused on systems for passenger vehicles, commercial buildings, and small handheld devices. These applications typically require power outputs that are either greater than 100 kW or less than 20 W, and a gap remains in developing viable fuel cell systems for applications requiring between 100 W and 100 kW. An integrated reformer fuel cell system has been developed for these medium power applications that utilizes a propane catalytic partial oxidation reformer coupled with a polybenzimidazole-based high-temperature proton exchange membrane fuel cell. After investigation into the requirements of military unmanned aerial systems (UASs), a system was designed to produce a net power of 250 W with a total mass of 2.23 kg and potential for 200-hour lifetime. The proposed design offers advantages over current UAS propulsion technologies because it is both quiet and capable of long duration flights, and also has advantages over other fuel cell systems as it is fueled with commonly available propane instead of high purity hydrogen.**

Keywords—high-temperature PEM fuel cell, propane reformer, catalytic partial oxidation, unmanned aerial system

I. INTRODUCTION

Our previous work has demonstrated the potential for combining a fuel reformer (to produce a hydrogen-rich gas) with a high-temperature proton exchange membrane (HT-PEM) fuel cell to deliver power outputs in the range of 200 – 500W [1-4]. Compared to other fuel cell systems, the HT-PEM platform benefits from the relatively high electrochemical efficiency (because of the direct conversion of chemical energy to electrical energy), and has the added advantage of being operable with a fuel stream that has high concentration of contaminants such as carbon monoxide. Using this foundational data, a practical fuel cell stack and mobile fuel cell system has been designed that combines a HT-PEM fuel cell with a propane catalytic partial oxidation (cPOx) fuel reformer for unmanned aerial system (UAS) applications.

The chosen application where a fuel cell device would provide several unique advantages is a mid-sized UAS (total weight < 55 lbs (25 kg), 6-10 ft (1.8-3 m) wingspan); these are mainly used in surveillance applications that require long endurance, but do not necessarily require high power densities for maneuverability. To further refine the target system requirements, the practical power, energy, and weight limitations for existing mid-sized UASs were researched in literature and through discussions with experts in the industry, to determine the practical design constraints for the fuel cell system focused on here.

Conventional UASs are typically powered using batteries or internal combustion engines (ICEs), which offer unique advantages but come with different drawbacks. ICEs are used to power most UASs with long-term surveillance missions because of the extended operation afforded when fueled with a hydrocarbon fuel. Some of these UASs can fly for over 24 hours between refueling times. However, UASs powered with ICE engines are often extremely noisy and therefore have to fly at high altitudes to ensure that those being surveilled cannot hear it approaching. These high altitude flights require expensive and complex optical equipment to properly view their targets from such far distances, and it is desirable to reduce the noise output of the propulsion system so that the flight altitude can be reduced and more cost-effective optics be used. Additionally, most ICEs require significant maintenance after each flight, typically with a major overhaul at 250 hours and a complete engine rebuild or replacement after 500 hours.

Batteries are the other primary propulsion technology for UASs and much quieter than ICE engines, thus allowing lower altitude flights and cheaper, less complicated optics. However, due to their low specific energy, they suffer from very short flight times that are typically no longer than 1.5 hours. Because fuel cells generate power without any moving parts and can be fueled with energy-dense hydrocarbon fuels, they offer quiet operation, long flight times, and less maintenance than current battery and ICE technology. A fuel cell propulsion system that reliably meets the target energy, power, weight, and durability requirements would provide substantial advantages for military UAS missions and other commercial applications. To date, however, few systems have been developed that meet the target requirements that would enable widespread adoption of fuel cells as the primary propulsion system for UASs.

II. HIGH-LEVEL STACK DESIGN

Although fuel cell UASs have previously been developed, many of the discussions with UAS operators indicated there is need for power plants that provide approximately 250 W of net power for propulsion. In setting the target weight and volume requirements, it was assumed that the balance-of-plant (BoP) equipment (electronic controller, air compressor, cooling fan, flow controllers, valves, and electronic control unit) consume approximately 20% of the total power output. Additionally, to be conservative, it was assumed that a full-sized fuel cell stack will generate a power density that is about 10% less than at the single cell level. Therefore, the gross power of the fuel cell

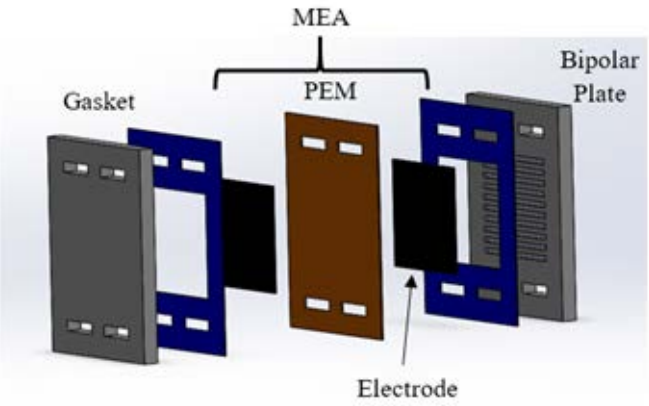

Fig. 1. Exploded view of a single fuel cell

stack should be designed assuming 30% will be lost, indicating that 360 W is needed to produce 250 W for the primary propulsion. With 250 W put towards the primary propulsion power plant, the UAS should weigh no more than 7.2 kg, and the fuel cell system including BoP equipment should weigh no more than 2.4 kg. Assuming a power density requirement of 58.3 W/liter, the total volume of the fuel cell stack and BoP equipment should be no more than 4.3 L.

Fuel cell stacks involve complex designs of bipolar plates, gaskets, and MEAs. The most common design is to stack a number of unit cells, shown in Figure 1, to achieve the desired voltage and power output level. Each component must be optimized so when assembled, the final completed stack will meet the target weight, durability, and volume constraints. To operate the HT-PEM fuel cell on reformate produced from propane cPOx with high power densities, operating temperatures of 200ºC are desired. At this temperature, operating pressures of 200 kPa have been shown to be effective for meeting the required minimum 200-hour durability metric.

Practical fuel cell systems are designed with a target stack voltage that is a few volts higher than the operating voltage of commonly available electronic equipment which tend to operate on voltages that are multiples of 12, i.e. 12V, 24V, 36V, etc. In this design, the primary application to power is a UAS electric motor that commonly operates on 12V. Thus, a target stack voltage of 14-16 volts is desirable. When operating on propane catalytic partial oxidation (cPOx) reformate, single HT-PEM fuel cell tests achieved a power density of approximately 240 mW/cm^2 at 200ºC, 200 kPa, and at a current density of 0.4 A/cm^2 at 0.6 V. Under these operating conditions, a 25 cell stack with an active area of 60 cm^2 per cell operating at 0.4 A/cm^2 and 0.6 volts would produce 360 W of power at 15 V and 24 A.

The H_2 flow to the stack will be generated from the fuel reformer however, the air required must be delivered at a pressure of at least 200 kPa in order to maintain the desired stack durability. Quite recently, a company was commissioned by the U.S. Department of Energy (DOE) to develop small, electronically actuated air compressors specifically designed for mobile fuel cell systems. One compressor listed with their available products is capable of providing around 50 SLPM of gas flow at a pressure ratio of 1.5, for around 80 W of power, where the compressor only weighs 110 g.

To ensure the cathode side of the stack is not over pressurized, a pressure regulator must be added to the system to ensure proper flow control. A few companies make small two stage pressure regulators that reduce inlet pressure up to 500 psi (3447 kPa) down to pressures around 20 psi (138 kPa). When combined with a 28 g flow regulator and 110 g air compressor, the entire air flow regulating system weighs 161 g. Overall, the mass of the compressor, air regulating equipment, and the interconnection piping is 189.8 g.

III. BIPOLAR PLATES AND FUEL CELL DESIGN

Based on extensive research and development in low-temperature (i.e., pure H_2) fuel cells, the most suitable bipolar plates for mobile HT-PEM fuel cells would be constructed from a stainless steel alloy (304 or 316L for example) and coated with a thin layer of gold to provide corrosion resistance. Additionally, a flow field design based on a serpentine pattern would provide the best possible performance, as low pressure drop and water management issues are not as great of a concern for HT-PEM fuel cells.

In most PEM fuel cell designs, two bipolar plate materials are bonded together to form cooling channels between. For the entire fuel cell stack, there are bipolar plates (formed by joining unipolar anode and cathode plates) between each pair of MEAs, and one unipolar plate at either end of the fuel cell stack. For a 25 cell stack, this amounts to a total of 24 bipolar plates and 2 unipolar plates. When considering bipolar plate designs found in patent literature such as [5], the surface area of the bipolar plate that is in contact with the active area of the MEA is approximately 88% of the total bipolar plate surface area. Assuming this same relationship applies to other bipolar plate designs, a 60 cm^2 MEA will require bipolar plates with total surface areas of 68.2 cm^2. If 0.25 mm thick sheet stock is used for the bipolar plate construction, then the total volume of each plate is 1.705 cm^3. Because stainless steel has a density of 8000 kg/m^3, the total mass of 24 bipolar plates and 2 unipolar plates is approximately 0.682 kg. If it assumed that the bipolar plates account for approximately 80% of the total weight of the stack as suggested in literature [6], then the total weight of a fuel cell stack that produces 360 W of power is approximately 853 g. If we add this to the air control hardware, including the air compressor, then the total weight of the system is now at 1,041.8 g.

IV. FUEL REFORMER

The proposed fuel reformer in this design utilizes a propane cPOx reaction. The primary advantage of using a cPOx fuel reformer is that it can be made very lightweight as only air flow, fuel flow, and operating temperature need to be controlled. A 25 cell stack with individual cell surface area of 60 cm^2 has a total stack surface area of 1500 cm^2 on either side of the MEA. Operating at a stoichiometric ratio of 1.5 at the anode requires 6.3 SLPM of H_2 flow. With the known conversion rates of propane cPOx, the reformer requires an

inlet flow of 1.57 SLPM (0.052 g/s) of propane to generate the necessary 6.3 SLPM of H_2. To maintain an O_2/C ratio of 0.53, air flow of 12.06 SLPM (0.26 g/s) is required.

The fuel reformer tested in this research program was built by PCI and uses the Microlith© design, which is essentially a stack of several wire meshes that have been impregnated with a catalyst. The reactor itself was only 31.75 mm in diameter, and 8.9 mm long. Although the weight of the reactor was unknown, other PCI reactors that are similar in diameter but four times greater in length are about 46 g [7]. A 5 cm long Inconel tube (density of 8193 kg/m^3) that would fit a 31.75 mm reactor with 2 mm thick walls weighs approximately 11.6 g, leading conservatively to a total fuel reformer mass of 57.6 g.

The proposed design schematic is illustrated in Figure 2. Given the mass of the fuel reformer, flow and pressure regulators, the entire proposed fuel reformer subsystem would have a mass of 138 g. For completeness, the weight for the additional piping used between components, and a thermocouple placed on the fuel reformer, should also be included. If there is approximately 2 cm of stainless steel tubing (8000 kg/m^3) connecting each component shown (6 connections), and assuming the same pipe dimensions of the fuel reformer, then the rest of the piping is approximately 11.6 g. If a 10 cm 14 gauge K-type thermocouple is used at the reformer, its mass will be 1.7 g. This brings the total fuel reformer fuel cell system mass up to 1,193.1 g.

V. CONTROL HARDWARE AND BOP

Beyond the solenoid valves needed as indicated in Figure 2, there is other BoP equipment necessary for durable operations, such as filters and check valves. In-line 60 micron cartridge filters used to remove particulates, such as the Swagelok SS-4F-T7-60, and the check valves, also made by Swagelok, have masses of 10 and 9.2 g respectively. These components have a total mass of 39.2 g. If it is assumed that there are 22 total piping connections within the whole system, each about 2 cm long with the same cross-sectional dimensions as the fuel reformer, then the total mass from piping connections in the entire fuel cell system is 99.5 g.

To maintain an operating temperature of 200ºC, the fuel cell stack will likely need additional cooling. Based on the known fuel cell electrochemical efficiency, for 360 W of electrical power generated by the fuel cell stack, an additional 306 W of heat will be generated. Assuming that cooling air used will be delivered at room temperature (20ºC), and the stack will be held constant at 200ºC, then the temperature difference is 180ºC. The specific heat capacity of air is 1005 J/(kg-K). With these assumptions, the air flow required is 5.07 m^3/hr (84.6 SLPM). A small 50 mm x 15 mm DC blower can be readily purchased [8], and is capable of 7.15 m^3/hr air flow, consuming only 1.68 W with a weight of 27 g.

To operate the valves and fans used during startup, operation, and shutdown, an electronic control unit (ECU) is necessary. The Arduino Uno is an ECU that is low weight, low cost, and easily programmable for the requirements needed in this design. Since the Arduino is not capable of reading K-type thermocouple measurements on its own, an additional thermocouple multiplexer board is required to effectively read the thermocouple signals. An Arduino K-type thermocouple multiplexer shield can be purchased which allows for the capacity of up to eight thermocouples to be read. Both of these boards weigh 25 g each for a total of 50 g.

In addition to controlling all of the actuated valves, the power output of the fuel cell must also be managed. Most often, DC-DC converters are used to regulate the power generated from the fuel cell before it is sent to the various loads. To estimate the realistic weight for a DC-DC converter, a commercially available converter manufactured by DROK that is capable of regulating 600 W of power was used as a model [9]. This converter maintains a constant voltage output and weighs approximately 221 g.

In addition to the fuel cell system, a practical UAS propulsion power plant design will likely be hybridized with a battery for load balancing and short bursts of power needed for climbing, maneuverability, and stabilization in the event of high winds. If it is assumed that in a worst-case scenario the battery will need to fully power the UAS for 15 minutes, the total capacity of the battery required is 90 Wh. Assuming state-of-the art Li-ion batteries with energy densities of 150 Wh/kg are used [10], then the mass of a 90 Wh battery is approximately 600 g.

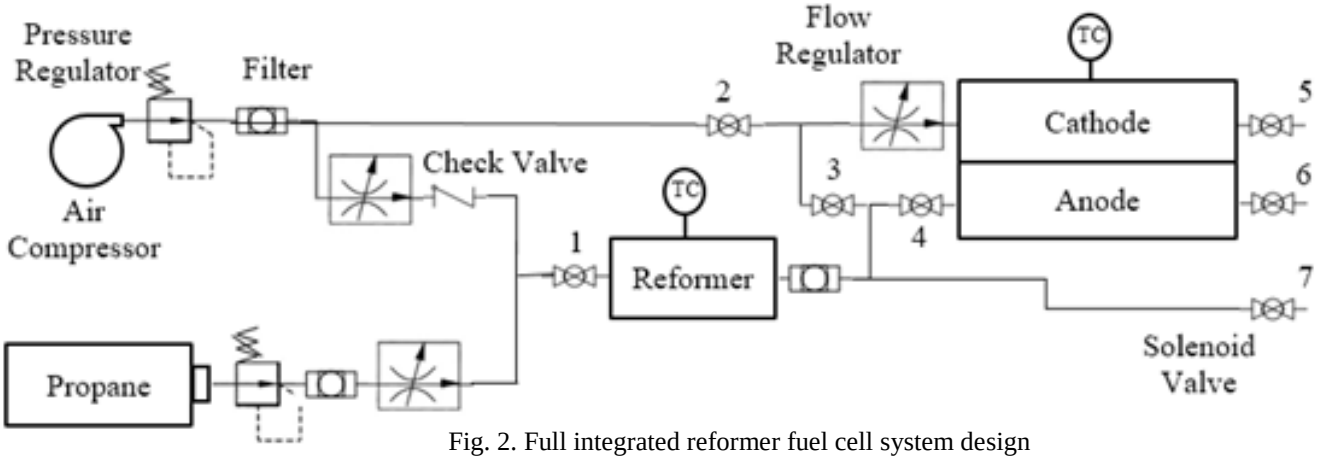

Fig. 2. Full integrated reformer fuel cell system design

Table 1 Component list for proposed fuel cell system

Component	Quantity	Total weight (g)
Air Compressor	1	110
Flow Regulator - Air	2	56
Flow Regulator - Propane	1	6.4
Pressure Regulator	2	46
Filter	3	30
Check Valve	1	9.2
Reformer	1	57.6
Solenoid Valve	7	59.5
Fuel Cell Stack	1	853
K-Type Thermocouple	2	3.4
Cooling Fans	1	27
ECU	1	58.5
DC-DC Converter	1	221
Piping	1	99.5
Battery	1	600
Grand total weight		**2237.1**

When adding up the estimated weight from all of the different components, the total mass of the proposed integrated reformer fuel cell system is 2.23 kg, which meets the 2.4 kg weight limit target described above. The breakdown of the different components and their weights are presented in Table 1.

The fuel cell stack accounts for the highest weight percentage at 38% followed by the battery at 27%. The next largest component is the DC-DC converter, and then the weight from piping and the air compressor are roughly the same. Although the total weight of the proposed system is less than the target maximum, further weight reductions could be expected with increased refinement of the battery chemistry, bipolar plate sheet stock thickness, BoP components, etc. These improvements will be considered as part of the ongoing engineering development of the baseline "alpha" prototype, which has been fabricated and tested in our laboratory (Figure 3). This initial design has demonstrated the viability of an integrated propane fuel reformer and HT-PEM fuel cell stack for UASs and other medium-power applications.

ACKNOWLEDGMENT

This work was performed under the financial assistance of award #70NANB14H262 from U.S. Department of Commerce, National Institute of Standards and Technology, which provided a Graduate Research Assistantship for Michael Waller.

REFERENCES

[1] M.G. Waller, M.R. Walluk and T.A. Trabold, "Performance of high temperature PEM fuel cell materials. Part 1: Effects of temperature, pressure and anode dilution," *International Journal of Hydrogen Energy*, Vol. 41, 2944-2954 (2016).

[2] M.G. Waller, M.R. Walluk and T.A. Trabold, "Operating envelop of a short contact time fuel reformer for propane catalytic partial oxidation," *Journal of Power Sources*, Vol. 274, 149-155 (2015).

[3] M.G. Waller, M.R. Walluk and T.A. Trabold, "Performance of a high-temperature proton exchange membrane fuel cell (HT-PEMFC) operating on simulated reformate," *Proc. ASME Power and Energy Conversion Conference*, Paper PowerEnergy2015-49562, San Diego, CA, June 28 – July 2, 2015.

[4] M.G. Waller, M.R. Walluk and T.A. Trabold, "Towards the development of a fuel cell system for residential applications: Propane reforming via catalytic partial oxidation," *Proc. ASME 12th Int. Fuel Cell Science, Engineering and Technology Conference*, Paper ESFuelCell2014-6431, Boston, MA, June 30 – July 2, 2014.

[5] J. A. Rock, H. Schlag, and K. R. Griffith, *Stamped fuel cell bipolar plate*. Google Patents, 2010.

[6] A. Kumar and R. G. Reddy, "Materials and design development for bipolar/end plates in fuel cells," *J. Power Sources*, vol. 129, no. 1, pp. 62–67, Apr. 2004.

[7] S. Roychoudhury, M. Castaldi, M. Lyubovsky, R. LaPierre, and S. Ahmed, "Microlith catalytic reactors for reforming iso-octane-based fuels into hydrogen," *J. Power Sources*, vol. 152, pp. 75–86, Dec. 2005.

[8] Gino, "Black Brushless DC Cooling Blower Fan 5015S 12V 0.14A 50mm x 15mm," *Amazon*, 21-Dec-2015.

[9] DROK, "DROK® 600W 12A DC Boost Voltage Converter 12-60V to 12-80V Step-up Power Supply Transformer Module Regulator Controller Constant Volt/Amp Car Regulated Laptop Battery Charger LED Driver Generator," *Amazon*, 21-Dec-2015.

[10] M. M. Thackeray, C. Wolverton, and E. D. Isaacs, "Electrical energy storage for transportation—approaching the limits of, and going beyond, lithium-ion batteries," *Energy Environ. Sci.*, vol. 5, no. 7, p. 7854, 2012.

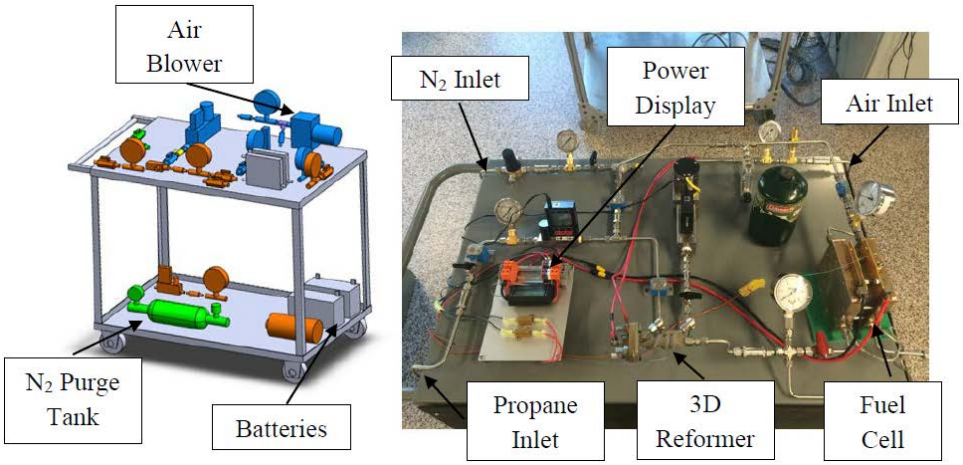

Fig. 3. Alpha prototype of integrated reformer and fuel cell system

Ultra Thin Solar Cell Used in UAVs Employing Surface Plasmon Polariton (SPP)

Richard Kyung, Ki Bum Baek, Alan Jaehyun Kim
Choice Research Group, Cresskill, NJ

Abstract— **New aerodynamic and material technology has enabled longer missions and increased payloads of the unmanned aerial vehicles (UAVs). To lengthen the battery life of the UAV, the objective is to develop a new breed of solar cells, which collects high energy trapped and absorbed in nano scaled metamaterial layer that would enable unrefueled flight. Employment of the metals and metal oxides, nano scaled cell system consisting of double and multiple layered photovoltaic devices in the solar cell was presented in this paper.**

The purpose of this research is to find practical metamaterials that can be used on the surfaces of fixed wing UAVs. The materials are composed of metals and dielectrics in which the surface plasmon polariton occurs when a beam of light is entered at a certain angle. In this paper, the reflection coefficient vs. angle for metamaterials are found through manual calculation and the use of computer programs. Also, surface plasmon polariton was created and the incident angle of the light wave and the effective index were calculated with the use of various metamaterials.

I. Introduction

The large surfaces on fixed wing UAVs can be used as a panel that can be composed of numerous solar cells. Recent improvements in solar cell and material technology is now enabling application of the solar power to UAVs of all sizes. High energy rechargeable SPP based battery is a new concept in battery technology for UAVs. Battery weight is incredibly reduced, enabling longer missions and increased payloads. The challenge presented in working with solar cells is collection of high light trapped and absorbed in a sub-absorption length-thick active layer, and replacement of the existing metamaterials with new materials used in thin-film devices. In this paper, we report a proposal of efficient solar cell employing SPP that can be applied to solar cell (SC), termed SC using plasmonic polariton, that offers a solution to all two issues with excellent performances.

Surface Plasmon Polariton (SPP) is infrared or visible-frequency electromagnetic waves, which travel along a metal-dielectric or metal-air interface. SPP will propagate along the interface until its energy is lost either to absorption in the metal or scattering into other decisions (1). These electromagnetic excitations or electromagnetic surface waves propagate in the perpendicular direction at the interface between a dielectric and a conductor, which are arisen via the coupling of the electromagnetic fields to oscillations of the conductor's electron plasma (3). This paper presented a nano scaled cell system consisting of monolayered photovoltaic devices. The basic element of the system is a surface plasmon polariton (SPP) based solar cell using a metals and metal oxides. In the SPP-employed solar cell, the optical strength can be maximized by adjusting the incident light, which resonantly excites an SPP mode in the absorption layer.

II. Numerical Analysis

A. Analysis and Procedure

With the use of COMSOL, the metamaterials with specific dimensions and indices of refractions were constructed, and then the photons passing through were simulated.

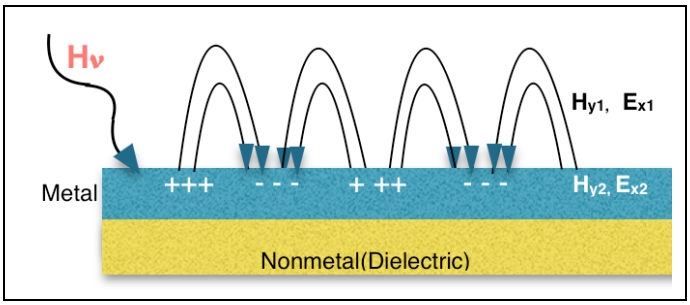

Fig.1 Surface Plasmon Polariton (SPP)

The Fig.2 below show the reflectivity of the light that has been propagated through the prism.

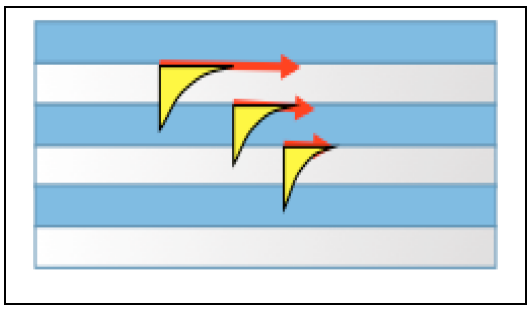

Fig. 2 Simulation Region for Surface Plasmon Polariton

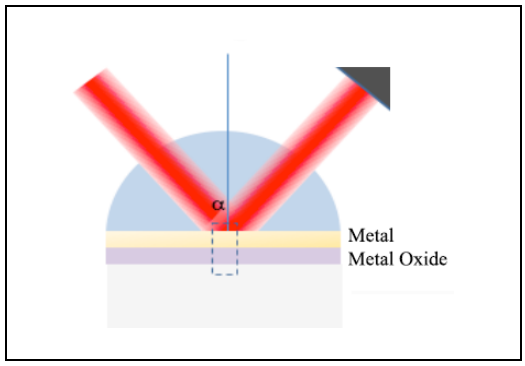

Fig. 3 Reflection of a Light with Wavelength (λ_0)

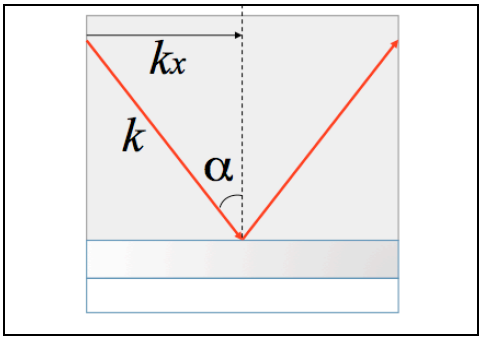

Fig. 4 Optimum Angle (α_{spp}) When Surface Plasmon Polariton Occures

The setup of the metamaterials consists of four major parts, which includes air, metal oxide, metal, and prism. Prism is an ideal object to use because it does not have any curvature in the reflection.

Underneath the parameter section, the refractive index for the prism, air, and dielectric and the thickness of the metal and the dielectric are determined initially. Then, the range of the incident angle (α) and the wavelength of the light are set. The calculation procedures are as follows:

1. Choose Wavelength of the incident ray: e.g. 550nm.
2. Select dielectric metal.
3. Select nonmetal.
4. Find approximate values of refractive index (n) and extinction coefficient (k) for both metals and nonmetals at certain wavelength.
5. Find Relative Permittivity of metal and nonmetal.
6. Find the incident angle in which the surface Plasmon polariton occurs.
7. Find the effective index.
8. Calculate the theoretical values of alpha and index.
9. Run the COMSOL for one period of metal and dielectric.
10. Repeat the steps above for the construction of a metamaterial with two periods with the same thickness and refractive index.

B. Result

In order to find the accurate incident angle (α) and the effective index, the point at which the reflectivity (the y-axis) reaches 0 must be found. This suggests that the light has not been reflected; instead, it travels directly parallel to the media inside.

For example, using silver, one can find a solution using these systems of equations:

C1. Silver Oxide

$$k_x = \{(E_1 \times E_2)/(E_1 + E_2)\}^{1/2} \times w/c \quad (1)$$

E_1 = Re (Permittivity of metal) = -13.67

E_2 = Permittivity of onide (dielectric) = 1

Where the effective index of refraction is defined by:

$$k_x/k_0 = \{(E_1 \times E_2)/(E_1 + E_2)\}^{1/2} \quad (2)$$

Using the geometry,

$$k_x = k \sin\alpha = nk_0 \sin\alpha \quad (3)$$

Finally, the optimum incident angle can be found using the the effective index of refraction,

$$n_{eff} = k_x/k_0 = n \sin\alpha \quad (4)$$

$$1.038 = 1.5 \sin\alpha \quad (5)$$

$$\alpha = 43.6°$$

C. Calculations

C1. Beryllium and Nonmetal Dielectrics

First, Beryllium combinations, such as Beryllium Tantalum Pentoxide, Beryllium Silicon Carbide Beryllium Niobium Pentoxide, Beryllium Cadmium Telluride, and Beryllium Aluminium Antimonide were analyzed.

The following Table I illustrates the results of optimum angle of SPP for one period of Beryllium and seven different nonmetals at 550nm.

TABLE I. DATA OF OPTIMUM ANGLES (°)

Metal	*Nonmetal*	*Optimum Angle α (°)*
Beryllium	Silver Oxide	43.6
Beryllium	Silicon Dioxide	35.2
Beryllium	Tantalum Pentoxide	39.9
Beryllium	Silicon Carbide	42.7
Beryllium	Niobium Pentoxide	40.4
Beryllium	Cadmium Telluride	41.9
Beryllium	Aluminium Antimonide	43.4

And the optimum incident angles for the Beryllium-Dielectric units are shown in Fig. 5 as follows:

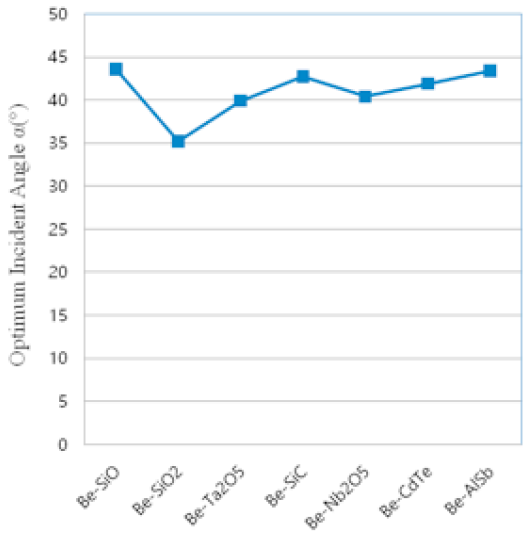

Fig. 5 Optimum Incident Angles for the Beryllium-Dielectric Units

C2. Iron and Nonmetal Dielectrics

Second, Iron Niobium Pentoxide, Iron Silicon oxide, Iron Silicon Dioxide, and Iron Tantalum Pentoxide are analyzed.

The Table II illustrates the results of optimum angle of SPP for the one period of Iron and five different nonmetal oxides at 550nm.

TABLE II. DATA OF OPTIMUM ANGLES (°)

Metal	Nonmetal	Optimum Angle α (°)
Iron	Molybdenum Trioxide	12.3
Iron	Niobium Pentoxide	12.4
Iron	Silicon Oxide	12.3
Iron	Silicon Dioxide	12.2
Iron	Tantalum Pentoxide	12.4

Fig. 6: Optimum Incident Angles for the Iron-Dielectric Units

C3. Vanadium and Nonmetal Dielectrics

Now Table III shows the optimum angle of SPP for the one period of other metals and nonmetal oxides calculated under 550nm.

Vanadium Silicon Oxide (500nm), Vanadium Silicon Dioxide (500nm), Vanadium Silicon Oxide (600nm), and Vanadium Silicon Dioxide (600nm) are analyzed

TABLE III. DATA OF OPTIMUM ANGLES (°)

Metal	*Nonmetal*	*Optimum Angle α (°)*
Vanadium (500nm)	Silicon Oxide	79.1°
Vanadium (500nm)	Silicon Dioxide	54.5°
Vanadium (600nm)	Silicon Oxide	73.8°
Vanadium (600nm)	Silicon Dioxide	53.7°

III. RESULT AND CONCLUSION

D. Result

In this research, various types of metamaterials were tested on COMSOL for their validity to use as solar device. Fig. 6 shows the relation of reflection coefficient vs. angle graph and the optimum incident angle for the copper-aluminum oxide combination is found to be 43.5 degree. As it is shown in the Fig. 7, the relation of Reflection Coefficient vs. Effective Index (k_x/k_0) is very similar to the patterns shown in the Fig. 18. They are similar because the angle and effective index are proportional to each other, as the incident angle α changes from 0 to 90 degree.

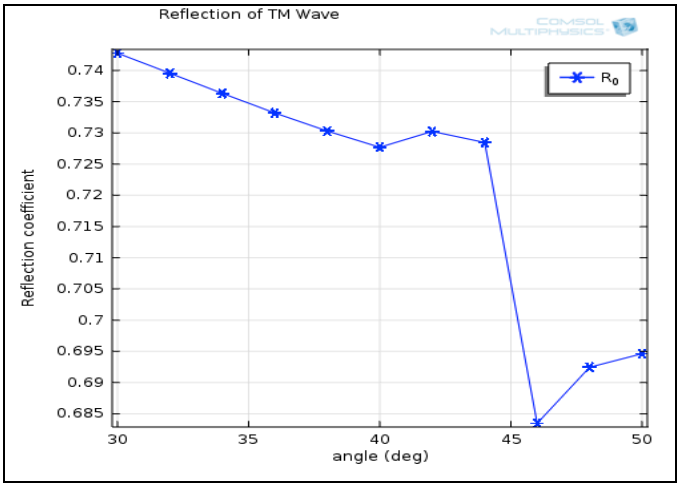

Fig. 6 Reflection Coefficient against Angle (deg) for Copper metamaterials

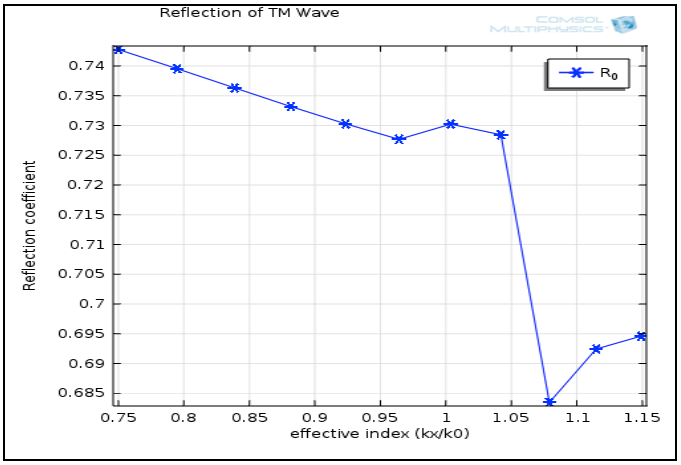

Fig. 7 Reflection Coefficient against Effective Index (k_x/k_0) for Copper metamaterials

Also, Fig.8 below shows the relation of the wavelength against effective index (k_x/k_0) for the copper-aluminum oxide combinations.

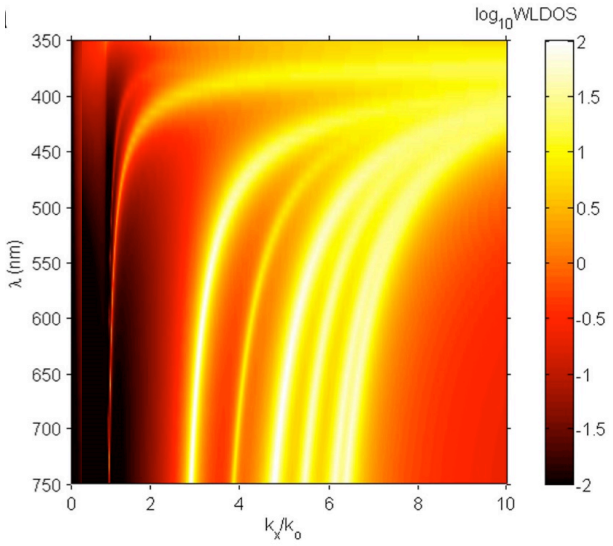

Fig. 8 Reflection Coefficient against Effective Index (k_x/k_0) for Copper metamaterials

B. Conclusion

Amongst the 47 metals that have dielectric constant, only Beryllium, Iron, Germanium, Silicon, and Tungsten with oxides combination(period) produced few optimum angles that are shown in Table I, II, and III. As the incident ray's wavelength was set as 550nm, twenty one metals like Calcium, Cerium, Erbium, Europium, Hafnium, Holmium, Iridium, Molybdenum, Niobium, Osmium, Praseodymium, Rhenium, Ruthenium, Scandium, Tin, Strontium, Tantalum, Thulium, Ytterbium, Zinc, and Zirconium could not be taken into account even though they express dielectric constant, as their range of wavelength does not include 550nm. For instance, Calcium's range of wavelength is from 0.001234 to 0.3163µm according to Rodriguez-de Marcos et al. 2015, and that of Iridium is from 0.667 to 286µm according to Ordal et al. 1988.

Metals including Aluminium, Gold, Bismuth, Cobalt, Chromium, Copper, Mercury, Indium, Lithium, Lutetium, Magnesium, Manganese, Sodium, Nickel, Lead, Palladium, Platinum, Rhodium, Titanium, and Vanadium did show dielectric constant at their certain range of light wavelength that included 550nm; however, when these metals were combined with five different oxides — Molybdenum Trioxide, Niobium Pentoxide, Silicon Oxide, Silicon Dioxide, Tantalum Pentoxide — at 550nm, there were no results exhibiting optimum angle.

Therefore, if the wavelength of the incident ray within the range of visible light varies approximately from 400 to 700nm, then more values of optimum angles for various combinations of metals and nonmetals that were not yet covered can be obtained.

N, the refractive index, was mainly set as 1.5, which is a refractive index for prism, because more optimum angles were observed when prism was used rather than air, whose refractive index is 1. Furthermore, when we set silver as metal and oxides as nonmetal to form a period at 550nm, we were not able to find an optimum angle for silver and oxides periods.

IV. Future Study or Applications

Employing other advanced techniques, one would be able to find better combinations of multilayered metals and metal oxides that can enhance the efficiency of the absorption in the solar cell devices. Also, physical and material properties of the dielectrics are needed to be studied in depth.

References

[1] Lemarchand, 2013. *Thin film; n,k 0.25-2.5 µm.* http://refractiveindex.info/

[2] Bright et al, 2013. *Nanocrystalline thin film; n,k 0.5-1000 µm* http://refractiveindex.info/?shelf=main&book=Ta2O5&page=Bright-nanocrystalline

[3] Larruquert et al, 2011. *Thin film; n,k 0.006154-131.7 µm.* http://refractiveindex.info/?shelf=main&book=SiC&page=Larruquert

[4] Lemarchand, 2013. *Thin film; n,k 0.25-25 µm.* http://refractiveindex.info/?shelf=main&book=Nb2O5&page=Lemarchand

[5] https://en.wikipedia.org/wiki/Surface_plasmon

[6] http://www.slideshare.net/dhruvinpatel549/plasmons-a-modern-form-of-super-particle-waves

[7] Treharne et al, 2011. *Thin film; n,k 0.3-1.5 µm.* http://refractiveindex.info/?shelf=main&book=CdTe&page=Treharne

Use of a UAV for Water Sampling to Assist Remote Sensing of Bacterial Flora in Freshwater Environments

Fernando Ontiveros, St. John Fisher, and Dylan Cornell, St. John Fisher

Ground truth data collection in bodies of water traditionally relies on the use of watercraft and manual sampling. The transport and cost associated with the use of this type of equipment, as well as the time required to reach the site of collection, may all be significantly reduced by the use of small unmanned aerial vehicles (UAV), or drones. In this project we evaluate the implementation of a modified UAV with the ability to collect a small volume of surface water up to 400m offshore. The bacterial flora found in the water of several locations in the Lake Ontario-Rochester Embayment area was recorded and entered into a multi-year database that attempts to correlate hyperspectral data obtained by the Landsat 8 Operational Land Imager with the isolated bacterial species. We found that water collection using a consumer grade UAV facilitated sampling efforts, saving time and providing easy access to otherwise difficult to reach collection sites.

System Modeling and Identification of Unmanned Quad Rotor Air Vehicle based on subspace and PEM

Liu Yi
School of Aerospace Engineering,
Beijing Institute of Technology,
Beijing, China
bjliuyi_2015@163.com

***Abstract*—In order to achieve accurate control of unmanned quad rotor air vehicle, the system model is in need. In this paper, the system model was built under the condition of the small angle hypothesis. Then, we combined the subspace state space system identification method and prediction error method (PEM) to the system identification of quad rotor air vehicle. By simulation, the flight dynamics model of unmanned quad rotor air vehicle example was successfully identified. The results showed that the proposed method had the advantage of both subspace state space system identification method and PEM, and it was always convergent and numerically stable.**

Keywords—quad rotor; subspace state space system; prediction error method; modeling; identification

I. INTRODUCTION

Unmanned quad rotor air vehicle has been rapid development in recent years. However, the manipulation of unmanned quad rotor air vehicle is more complicated than other types of unmanned air vehicle (UAV), which in a way hinder its development. Due to its incomparable advantages, such as hover, flight in various postures, able to adapt to various environments, independent takeoff and landing capability, height intelligent, able to complete the flight mission in a confined space, it will have broad application prospects.

Unmanned quad rotor air vehicle is typical underactuated system, which means that the number of control input is less than that of its degrees of freedom. It has six space degrees of freedom, while has only four inputs from the four rotors whose rotating speed control the flight of the unmanned quad rotor air vehicle. This system is characterized by the nonlinear coupling between the direct input portion and the underactuated portion. Thus, it is difficult to obtain accurate flight dynamics modeling of the unmanned quad rotor air vehicle.

Mechanism modeling and system identification modeling are main flight dynamics modeling of the unmanned quad rotor air vehicle. Mechanism modeling needs to use experimental methods to make up for lack of aerodynamic calculations, and its accuracy of the model parameters is not high. While system identification modeling uses the external characteristics of the inputs and outputs to find an equivalent input-output model. Hence system identification modeling has more adaptive to the environment and obtain better accuracy over a wide range than the traditional mechanism modeling. Due to these advantages, the system identification modeling is used widely in the flight dynamics modeling of the unmanned helicopter. Gain tuning process of cascade controller was discussed and transfer functions of the quad-rotor system were identified using system identification and parameter estimation [1]. System identification of lateral and longitudinal dynamics were presented for an ARF-60 UAV using both linear and nonlinear estimation methods which were Autoregressive with exogenous model method for linear estimation, and Hammerstein-Wiener method for nonlinear estimation [2]. The authors applied Mean-squared error (EWC) in the system identification of real self-developed UAV's takeoff motion, and compared the result of EWC-LMS with traditional LMS (least mean square) and TLS (total least square) [3].

Predictive error method (PEM) and subspace identification method are two common methods in Time domain identification. Due to the high precision, PEM has broad scope of application [4]. But the initial state can greatly influence the performance of PEM. When the initial state is not ideal, PEM has low precision, and high computational complexity. Subspace identification method is used for linear time-invariant, multi-input multi-output system. It integrates system theory, linear algebra and statistics, and directly uses the input-output data to estimate state space model for multivariable system identification [5]. Since the subspace algorithm doesn't solve the problem in accordance with an optimal criterion, it is suboptimal. For any controllable and observable linear system, the subspace identification method only assumes the noise and input system are independent, which is difficult to meet in the actual system. Thus, the accuracy of the subspace identification method is not high.

This paper builds a linear system model with small angle assumption, and uses the combination of the subspace identification method and the PEM to identification of the unmanned quad rotor air vehicle. The subspace identification method is used to obtain a suboptimal initial model. Then, the PEM is used to get high accurate identification.

II. SYSTEM MODEL

The flying schematic diagram of quad rotor air vehicle is shown in Figure 1. It has four symmetric rotor, wherein two

rotors as one group. The opposing two rotors turning identically while the adjacent two rotors turning oppositely.

When the UAV is in hover state, four rotors have the same speed, generating the force that offsets the gravity of UAV. Meanwhile, because of its symmetry, the anti-twist torque is offset and the stable hover is achieved. Increasing or decreasing the speed of four rotors can complete VTOL function. When increasing the speed of one rotor alone, UAV can pitch and roll; when increasing the speed of two rotors in same group can achieve the yaw movement.

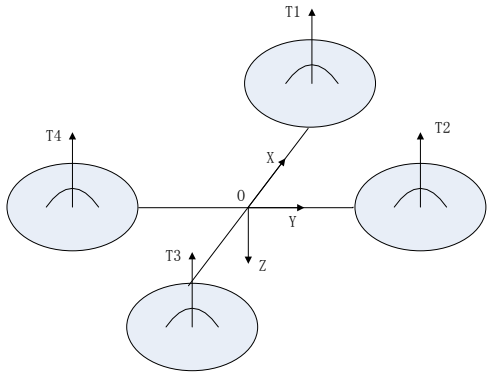

Fig. 1. The flying schematic diagram of quad rotor air vehicle.

UAV can be regarded as a rigid body motion with six degrees of freedom under the condition of regardless of the elastic deformation and vibration. Normally, many complex factors should be considered, such as effect of airflow which includes the resistance and lateral torque of UAV in addition to the rotor's lifting force and overturning moment. These moments are not only in relationship with the airflow, but also with the geometrical characteristics of UAV. Hence, to provide a more accurate identification of the model, the following limited condition is made in the mechanical analysis: UAV is in a windless environment, and the state of the UAV is in hover or slow flight status. Here, we made the following assumptions: (a) lifting force produced by rotors is proportional to the speed, ignoring waving of rotor; (b) Euler angle rate and the angle rate of the body coordinate system can be seen as consistent, since the state of UAV changes very little when in hover state; (c) the center of UAV is regarded as its center of mass.

In the hover state of quad rotor air vehicle, rotors are only affected by the upward force and anti-twist torque, hence, the force and torque can be approximately proportional to the square of the rotor speed, the scale factor is K_t, K_m. The combined force and torque of the system are as follows:

$$\begin{bmatrix} F_x \\ F_y \\ F_z \end{bmatrix} = m \begin{bmatrix} 0 \\ 0 \\ g - K_t\left(\Omega_1^2 + \Omega_2^2 + \Omega_3^2 + \Omega_4^2\right) \end{bmatrix} \tag{1}$$

$$\begin{bmatrix} M_x \\ M_y \\ M_z \end{bmatrix} = \begin{bmatrix} (T_4 - T_2)l + \sum_{i=1}^{4} \tau_x \\ (T_1 - T_3)l + \sum_{i=1}^{4} \tau_y \\ \sum_{i=1}^{4} M_i \end{bmatrix} \tag{2}$$

Selecting the rate of three axes and Euler angle rate as the state quantity of the system and the speed of four rotors as input, a simplified kinetic model can be obtained:

$$\begin{cases} \ddot{x} = -\dfrac{K_t}{m}(\sin\psi\sin\phi + \cos\psi\cos\phi)U \\ \ddot{y} = -\dfrac{K_t}{m}(\cos\psi\sin\phi + \sin\psi\cos\phi)U \\ \ddot{z} = g - \dfrac{K_t}{m}(\cos\theta\cos\phi)U \end{cases} \tag{3}$$

$$\begin{cases} \ddot{\phi} = \dot{\theta}\dot{\psi}\left(\dfrac{I_y - I_z}{I_x}\right) + \dfrac{lK_t}{I_x}\left(\Omega_4^2 - \Omega_2^2\right) - \dfrac{\tau_x}{I_x} \\ \dot{\theta} = \dot{\phi}\dot{\psi}\left(\dfrac{I_z - I_x}{I_y}\right) + \dfrac{lK_t}{I_y}\left(\Omega_1^2 - \Omega_3^2\right) - \dfrac{\tau_y}{I_y} \\ \dot{\psi} = \dot{\phi}\dot{\theta}\left(\dfrac{I_x - I_y}{I_z}\right) + \dfrac{K_m}{I_z}\left(\Omega_1^2 - \Omega_2^2 + \Omega_3^2 - \Omega_4^2\right) \end{cases} \tag{4}$$

Where I_x, I_y, I_z represent the inertia of three axes respectively, l is the distance between the center of mass and the center of the rotor, m represents the mass of the aircraft. τ is the effect produced by the gyroscopic effect of the motor and calculated as follows:

$$U = \Omega_1^2 + \Omega_2^2 + \Omega_3^2 + \Omega_4^2 \tag{5}$$

$$\tau_x = \dot{\theta} J_r\left(\Omega_1 - \Omega_2 + \Omega_3 - \Omega_4\right) \tag{6}$$

$$\tau_y = \dot{\phi} J_r\left(\Omega_1 - \Omega_2 + \Omega_3 - \Omega_4\right) \tag{7}$$

Where Jr is the moment of inertia.

III. IDENTIFICATION METHOD

After building the system model under the condition of the small angle hypothesis, the subspace state space system identification method and PEM are combined to the system identification of quad rotor air vehicle. Using the subspace state space system identification method to obtain a suboptimal initial model, then, use the PEM algorithm to achieve a more accurate identification.

A. The Subspace State Space System Identification Method

Based on the kinematic equation of helicopter, linear rigid body model with six degrees of freedom can be obtained around the trim state [6].

$$\begin{cases} \dot{x} = Ax + B\mu \\ y = Cx \end{cases} \tag{8}$$

where

$$x=\begin{bmatrix}u & v & w & p & q & r & \phi & \theta & \psi\end{bmatrix}^T$$

$$y=\begin{bmatrix}u & v & w & p & q & r & \phi & \theta & \psi\end{bmatrix}^T$$

$$A=\begin{bmatrix}X_u & X_v & X_w & X_p & X_q & X_r & X_\theta & X_\phi & X_\varphi\\ Y_u & Y_v & Y_w & Y_p & Y_q & Y_r & 0 & Y_\phi & Y_\varphi\\ Z_u & Z_v & Z_w & Z_p & Z_q & Z_r & Z_\theta & Z_\phi & 0\\ L_u & L_v & L_w & L_p & L_q & L_r & L_\theta & L_\phi & 0\\ M_v & M_v & M_w & M_p & M_q & M_r & M_\theta & M_\phi & 0\\ N_v & N_v & N_w & N_p & N_q & N_r & N_\theta & N_\phi & 0\\ 0 & 0 & 0 & 0 & 1 & 0 & 0 & 0 & 0\\ 0 & 0 & 0 & 1 & 0 & 0 & 0 & 0 & 0\\ 0 & 0 & 0 & 0 & 0 & 1 & 0 & 0 & 0\end{bmatrix}$$

$$B=\begin{bmatrix}X_a & Y_a & Z_a & L_a & M_a & N_a & 0 & 0 & 0\\ X_e & Y_e & Z_e & L_e & M_e & N_e & 0 & 0 & 0\\ X_r & Y_r & Z_r & L_r & M_r & N_r & 0 & 0 & 0\\ X_c & Y_c & Z_c & L_c & M_c & N_c & 0 & 0 & 0\end{bmatrix}^T$$

Where, u, v, w represent the component of the speed V in the body coordinates x, y, z axis respectively; ϕ,θ,ψ are the roll angle, pitch angle, yaw angle respectively; p, q, r are roll rate, pitch rate, yaw rate respectively; $\mu=\begin{bmatrix}\delta_a & \delta_e & \delta_r & \delta_c\end{bmatrix}^T$, $\delta_a,\delta_e,\delta_r,\delta_c$ represent longitudinal cyclic pitch, lateral cyclic pitch, collective pitch and tail rotor pitch respectively; C is Identity matrix.

B. PEM Identification Method

Considering a more general model as follows:

$$Z(k)=f\left(Z(k-1),...,Z(1),Z(0),u(k-1),...,u(1),u(0),\theta\right)+e(k) \quad (9)$$

Where, Z (k) is the output vector with dimension m; u (k) is the input vector with dimension r; θ is the model parameter vector; e (k) is the noise term with mean zero, $\sum_e$ is covariance matrix; Z(0) is the initial state of the output and is necessary to calculate Z(1).

Set

$$Z^{(k-1)}=[Z^T(k-1),\ldots, Z^T(1)]T,\ u^{(k-1)}=[u^T(k-1),\ldots,u^T(1)]^T \quad (10)$$

The formula can be rewritten as:

$$Z(k)=f\left(Z^{(k-1)},u^{(k-1)}\theta\right)+e(k) \quad (11)$$

After obtaining the date $Z^{(k-1)}$ and $u^{(k-1)}$, the best forecast of output Z(k) is taking its conditional mathematical expectation:

$$\hat{Z}(k\mid\theta)=E\left\{Z(k)\mid Z^{(k-1)},u^{(k-1)},\theta\right\} \quad (12)$$

Making

$$E\left\{\left\|Z(k)-\hat{Z}(k\mid\theta)\right\|^2\right\}=\min \quad (13)$$

Obviously, this best output forecast should be the output of best model. This can be obtained by minimizing the prediction error criterion. Two common prediction error criteria are as follows:

$$\begin{cases}J_1(\theta)=Tr[WD(\theta)]\\ J_2(\theta)=\log[\det D(\theta)]\end{cases} \quad (14)$$

Where

$$D(\theta)=Z(k)-f\left(Z^{(k-1)},u^{(k-1)},\theta\right)$$

Weighting matrix W is preselected definite matrix; when $L\to\infty$, $D(\theta)$ will converge to the covariance matrix of e (k). Usually, parameter estimates obtained by minimization principle $J_1(\theta)$ or $J_2(\theta)$ using Newton-Raphson are called prediction error estimate.

C. The Improved Identification Method

The improved identification method in this paper is as follows:

(a) Using the subspace identification method to obtain the initial model of the system. The derivation of the subspace identification method can be referred to literature [7].

(b) As linear equations of unmanned helicopter have structural requirements, part parameter values of A, B in formula (8) are defined. Then use the initial model obtained by subspace identification method as the initial state of PEM. This method can greatly improve the accuracy of identification.

IV. Experiments

A. Data Preprocessing

To accurately identify the model parameters and avoid putting the noise of the system into the model, we need to filter the obtained flight data. As majority of the noise of UAV is at high frequency band and its natural frequency is usually at 5Hz, low-pass filtering of identified data is in need to eliminate high-frequency component of output signal and optimize the identification results. We adopted the 4th order Butterworth lowpass filter with 8 Hz cut-off frequency.

In the simulation, trying to reflect the higher vibrational levels, strong low-frequency noise is added to both the identification inputs and outputs. Take the single channel sweep input as input stimulus. After data screening and filtering, the main parameters A and B are obtained.

$$A=\begin{bmatrix}-176.8 & -32.9 & -719.5 & -477.3 & 202.3 & 8183.6 & 3.92 & 1426.91 & -1.15\\ 565.7 & 104.8 & 2330.4 & 1592.4 & -737.5 & -2753.2 & 0 & -4773.1 & -7.42\\ 3.8 & 0.2 & 21.3 & 26.8 & -13.8 & -382.3 & 3.8 & -57.1 & 0\\ 111.5 & 22.3 & 449.3 & 282.2 & -127.9 & -5114.1 & -1.9 & -897.4 & 0\\ 37.4 & 6.9 & 137.4 & 64.1 & -32.2 & -1298.9 & -4.7 & -245.2 & 0\\ 34.3 & 7.1 & 141.5 & 92.9 & -41.8 & -1636.9 & -0.9 & -285.1 & 0\\ 0 & 0 & 0 & 0 & 1 & 0 & 0 & 0 & 0\\ 0 & 0 & 0 & 1 & 0 & 0 & 0 & 0 & 0\\ 0 & 0 & 0 & 0 & 0 & 1 & 0 & 0 & 0\end{bmatrix}$$

$$B = \begin{bmatrix} 2079.2 & -6937.1 & -88.9 & -1291.3 & -349.8 & -413.9 & 0 & 0 & 0 \\ 108.1 & -256.9 & 6.8 & -63.4 & -26.9 & -18.5 & 0 & 0 & 0 \\ -4511.3 & 15014.2 & 183.4 & 2815.2 & 724.3 & 887.2 & 0 & 0 & 0 \\ 522.0 & -1698.6 & -18.5 & -321.9 & -85.7 & -108.3 & 0 & 0 & 0 \end{bmatrix}^T$$

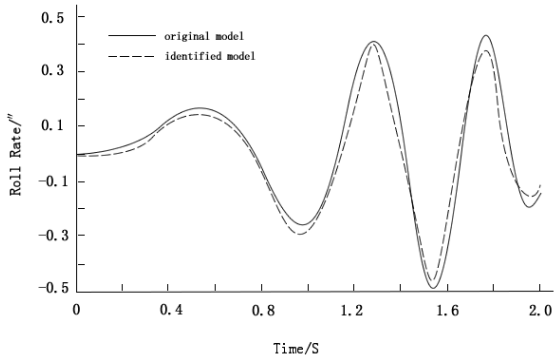

Fig. 2. Comparisons of roll rate outputs of original and identified models.

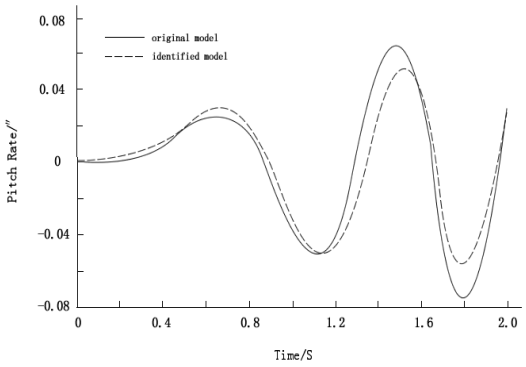

Fig. 3. Comparisons of pitch rate outputs of original and identified models.

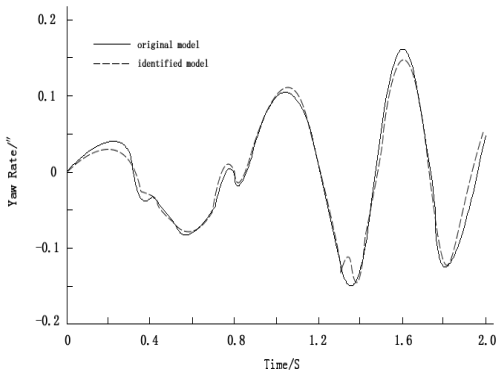

Fig. 4. Comparisons of yaw rate outputs of original and identified models.

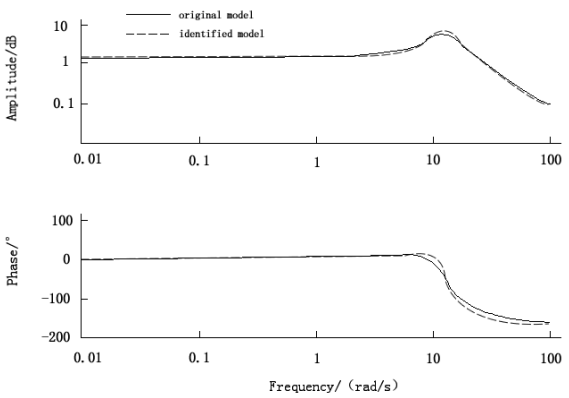

Fig. 5. Frequency-response of lateral input to roll rate.

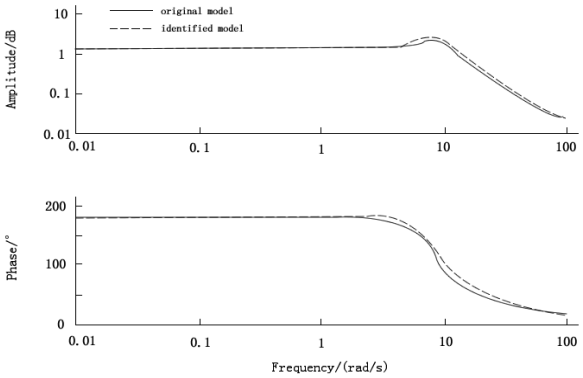

Fig. 6. Frequency-response of longitudinal input to pitch rate.

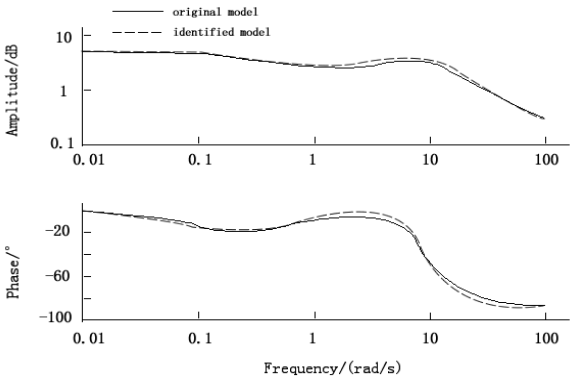

Fig. 7. Frequency-response of yaw input to yaw rate.

The system model in hover state is obtained by identification methods, simulations should be done to verify whether it can fully reflect the characteristics of the system. There are two methods to verify: time domain and frequency domain. A set of input-output data which is not used to identification is needed in time domain method. Using the identification results to simulate and compare the coincidence degree of identified output and original output with the same input. Comparisons of identified output and original output in

the time domain are shown in Figure 2-4, while comparisons of identified output and original output in the frequency domain are shown in Figure 5-7.

V. CONCLUSIONS

Based on the analysis of the advantages and disadvantages of the subspace state space system identification method and PEM, we proposed an identification method which combined the two mentioned methods and applied it to the identification of unmanned quad rotor air vehicle. The proposed method is characterized by its strong robustness and is suitable for identifying instable flight dynamics model of unmanned quad rotor air vehicle. Simulation results show that our method can identify the flight dynamics model of unmanned quad rotor air vehicle in hover state under the condition of high noise level.

References

[1] M. Harun-Gr-Rashid, J.B. Song, Y.S. Byun, et al., "System identification and parameter estimation of a multi-rotor flying machine," IEEE 2015 15th International Conference on Control, Automation and Systems, 2015, pp. 1052-1057.

[2] B. Khalil and A. Yesildirek, "System identification of UAV under an autopilot trajectory using ARX and Hammerstein-Wiener methods," IEEE 2010 7th International Symposium on Mechatronics and its Applications, 2010, pp. 1-5.

[3] Z. Zhou, J. Hu, S. Liu, et al, "System identification of UAV based on EWC-LMS," IEEE 2006 IMACS Multiconference on Computational Engineering in Systems Applications, 2006, pp. 721-726.

[4] F. Yang, X. Xiong, Z.G. Chen, et al, "Modeling, system identification and validation of small rotorcraft-based unmanned aerial vehicle," Journal of Beijing University of Aeronautics and Astronautics, vol. 36, no. 8, 2010, pp. 913-917.

[5] Y.F. Li, H.Y. Su and J. Chu, "Overview on subspace model identification methods," Journal of Chemical Industry and Engineering (China), vol. 57, no. 3, 2006, pp. 473-479.

[6] B. Mettler, M. B. Tischler and T. Kanade, "System identification of small-size unmanned helicopter dynamics," Annual Forum Proceedings-American Helicopter Society, 1999, pp. 1706-1717.

[7] W. Favoreel, B. De Moor and P . Van Overschee, "Subspace state space system identification for industrial processes," Journal of Process Control, vol. 10, no. 2, 2000, pp. 149-155.

Benewake's LiDAR Products Introduction

York Chen, Benewake

Benewake CO., LTD is a high-tech company that focuses on “Robots’ eyes”. The company received series A round investment from IDG Ventures. Benewake aims to develop commercial LiDAR and therefore bring intelligent robots into thousands of households. Benewake’s “Robots’ eyes” product, the IR DE-LiDAR (based on ToF) is mainly used for drones, Robotics, and Driverless Automobiles to meet the requirements of auto-avoidance, simultaneous localization and mapping (SLAM), terrain following, and RGBD object recognition.

A Simple and Effective Semi-supervised Learning Framework for Hyperspectral Image Classification

Ahmed Elshamli, Graham W. Taylor, Shawki Areibi
School of Engineering, University of Guelph, Guelph, Canada
{ashamli,gwtaylor,sareibi}@uoguelph.ca

***Abstract*—Semisupervised learning (SSL) is often used when the number of labeled samples is very small compared to the number of unlabeled samples. It permits the exploitation of structure within unlabeled samples during the learning task. Like many other applications, remote sensing images suffer from the limited number of ground-truth samples and therefore semisupervised techniques may be used to overcome this limitation. In this paper, a semisupervised framework is proposed for classification of hyperspectral images with scarce labeled samples. Our method, which we call SSL-CC, utilizes fuzzy spectral clustering to label spatially neighboring samples. SSL-CC is implemented and tested on two benchmark hyperspectral datasets. Fuzzy clustering is compared to traditional crisp clustering (k-means) and the obtained results indicate that fuzzy clustering can significantly improve classification accuracy. SSL-CC achieves on average 60% improvement over a baseline SVM classifier.**

***Index Terms*—Hyperspectral imaging; semisupervised learning; classification; spatial correlation, machine learning; clustering**

I. Introduction

Remote sensing is the science and technology of obtaining information about objects from a distance, typically from satellite, aircraft or an unmanned aerial system (UAS). As technology improves and evolves, remote sensing data becomes richer in all domains: spectral, spatial, and temporal. For example, hyperspectral images (HSI) are remote sensing images that measure electromagnetic signals reflected from the surface at a narrow wavelength range [1]. In this case, a specific ground pixel could have a few hundred measurements, each representing the electromagnetic reflection at different wavelengths. Furthermore, these images are usually taken at a high ground resolution, and frequently repeated over time (i.e. captured as a time series). Manual analysis of HSI cannot be easily performed by humans; therefore automated systems are being deployed to accomplish this complex task. As a result, several machine learning algorithms have been utilized to carry out different analysis tasks [2] such as pixel-based classification.

In the last few decades, classification has been extensively studied within the machine learning community, and several novel algorithms and techniques have been proposed [3]. The performance of these classification algorithms heavily depends on the quality and the quantity of the training set. As the name implies, the training set is used by the classification algorithm to learn how to distinguish between the classes; therefore, this set must include the class tag or *label* for every data record within the set. It is common in remote sensing to perform a pixel-based classification, that is assigning every pixel in the input with a category. Obtaining a large and high-quality ground-truth labels for such tasks is non-trivial; moreover, the cost and time needed to annotate data is formidable if a comprehensive field campaign is used to obtain this set.

The classification task, in general, is difficult in terms of time and computational cost. The difficulty of this task becomes more challenging as the data dimension increases such as the electromagnetic measurements in HSI. In addition to the challenge of high dimensionality, classification performance is highly affected by noise and uncertainty in the data. By default, all of these challenges exist in HSI since the number of spectral bands is large, and these images are naturally noisy due to many factors such as atmospheric condition and pixels which represent mixtures of different materials [4]. As noted above, unlike traditional image classification which associates each image with single class label; we consider a pixel-based classification where each pixel is associated with its corresponding class label. In addition to annotation costs already noted, pixel-based classification (also known as semantic segmentation) is more challenging and computationally demanding compared to traditional classification.

These challenges have motivated us to develop a semisupervised classification framework (abbreviated as SSL-CC) that utilizes complimentary unlabeled data to overcome the problem of limited training data and therefore enhance the final classification results. SSL-CC is based on two observations: i) Similar samples tend to generate "clusters" in feature space [5], ii) Spatially neighbouring pixels are more likely to belong to the same class. In this work, fuzzy clustering is used to compute the cluster membership values for all image pixels, followed by a labeling step to assign "pseudo-labels" to the unlabeled samples. A classifier is then built using a new training set produced by combining the available ground-truth with spatially neighbouring pixels which have been assigned pseudo-labels. Our main contributions are summarized as follows:

- We propose a simple and generic framework that utilizes a very small number of ground-truth samples to boost the performance of pixel-based HSI classification.
- We analyze the effects of crisp vs. fuzzy clustering on the quality and quantity of the generated pseudo-labels.

The remainder of this paper is organized as follows. Section II provides a review of related work. Section III details

our proposed methodology. The experimental setup and results obtained are presented in section IV. Finally, Section V provides concluding remarks and future directions.

II. Related work

Early SSL techniques that have been proposed to classify remote sensing images have failed to exploit spatial relationships and typically have relied on generative models which assume that the data is generated from a statistical distribution with unknown parameters. Therefore, these approaches aim to estimate the distribution parameters by utilizing only the spectral characteristics of these images [6]. The high performance achieved by the support vector machines (SVM) for remote sensing have led to many SSL variants [7]. Spatio-spectral SVM based techniques have been developed and applied to HSI, for example, the Transductive SVM (TSVM) [8] and Laplacian SVM (LapSVM) [9].

Several clustering techniques have been also exploited. Tuia et al. [10] proposed a SSL method which builds the SVM kernel based on multiple k-means clustering. Tarabalka et al. [11] propose the use of a clustering map to refine the results of a classifier trained on the spectral space. Alok et al. [12] use Fuzzy C-means (FCM) [13] clustering, adding samples with highest membership values to the ground-truth. However, the spatial information has not been incorporated in this work. FCM has been also used as a semi-supervised tool to increase the training set size of a probabilistic SVM [14]. Also in this work only the spectral information has been used to increase the training set size.

It is clear that incorporating spatial information improves classification performance. Unlike most of the previous work which is iterative and relies on the performance of the classifier using the initial ground-truth; the proposed framework in this paper is not iterative and does not rely on the initial classification performance. Furthermore, the proposed framework utilizes the cluster fuzziness to overcome the uncertainty and the noise present in remote sensing images.

III. The Proposed Framework

The overall proposed framework, SSL-CC, is presented in Fig. 1. The input HSI is assumed to have the following characteristics:

- HSI: $\Re^{(M\times N)\times D}$; Where M, and N are the spatial resolution, and D is the spectral resolution,
- Number of classes: C, and
- Ground-Truth labels: $T(K)$ (K samples with their associated class labels).

The main components of the system are explained next.

A. Clustering

In this study, two clustering techniques are considered, k-means and FCM. Both techniques are iterative and they cluster the data based on similarity. For real numbers, squared Euclidean distance is typically employed to calculate the similarity between the samples. Both techniques normally start by setting an arbitrary mean for each cluster. The iterative process

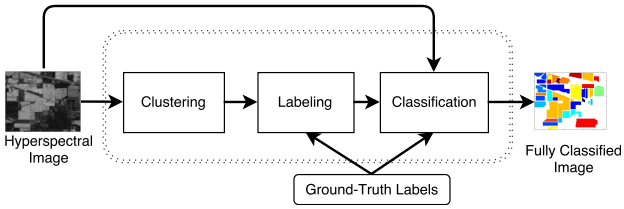

Fig. 1. The proposed framework

consists of the following two steps. i) The assignment step: the distance between the means and all the samples are calculated and each sample is then assigned to the nearest mean. ii) Means update: each cluster mean is recalculated to be the mean of the samples assigned to it. K-means is a hard clustering technique, where each sample is considered to belong to only one cluster. On the other hand, FCM clusters the samples to belong to all the clusters with different degree of membership. This key difference reflects the basis of the assignment and the update steps. Each sample is assigned to all the clusters based on its distance from their means; a high degree of membership is assigned to the cluster with nearby means and a small degree of membership to distant clusters. Likewise, the means are updated to reflect this relation between the mean of each cluster and the membership value of each sample. Membership values for each sample are normalized to sum to unity. This iterative process terminates when there is no significant change for the cluster means during the last few iterations.

SSL-CC clusters all the image pixels using only the spectral space, and the number of clusters is set to the actual number of classes provided with the input image.

B. Labeling

The labeling algorithm is summarized in Algorithm 1. The algorithm inputs are the original ground-truth labels, the clustering results, and two user-defined parameters: the size of the window for which neighbours are considered (W), and the threshold value (τ). Since FCM associates each pixel to all clusters with varying membership values, the degree of membership is presented in the matrix $\mu^{(M\times N)\times C}$, where $\mu(i,j)$ represents the associated membership value of pixel i for cluster j.

Initially, the pseudo-label set is initialized as an empty set (step 1) and then for every pixel (p) in the ground-truth set (step 2,3) the following procedure is performed: (step 4) the cluster of p is determined by finding the cluster with maximum membership value, then all the neighbors of p are checked if they belong to the same cluster as p (step 6). The neighbors which belong to a cluster are decided based on the membership value and the supplied threshold parameter τ. In the case of k-means the same condition can be applied since the degree of membership will either be 0 or 1. Neighbors satisfying this condition are added to the pseudo-label pool (step 7). The maximum number of neighboring pixels to be checked for p is governed by W, and is equal to $\left[(2W-1)^2-1\right]$.

As W grows, the windows for different ground-truth pixels may overlap, resulting in pixels from different classes being

assigned the wrong pseudo-label. To avoid this, generated pseudo-labels are checked for disagreement and pixels with conflicting pseudo-labels are removed from the set (step 11).

Algorithm 1 The labeling procedure

Input: Ground-Truth, $\mu(i,j)$, W, τ
Output: P-Labels
1: P-Labels = $\{\}$;
2: **for** All available Ground-Truth samples (i) **do**
3: p = GroundTruth(i);
4: Cluster = FIND(MAX($\mu(p)$))
5: **for** All neighbours (k) of p within W **do**
6: **if** $(\mu(k, Cluster) \geq \tau)$ **then**
7: P-Labels = P-Labels $\cup$ (class(j) $\leftarrow$ class(p))
8: **end if**
9: **end for**
10: **end for**
11: P-Labels = Remove Disagreement (P-Labels)
12: **return** P-Labels

C. Classification

The training set consists of the originally supplied ground-truth labels and the produced pseudo-labels. A SVM classifier is then trained using this training set to predict the class labels for the remaining unlabeled samples. The final accuracy of the system is calculated using the confusion matrix computed using both the classifier result and the pseudo-labels.

IV. Results

We conduct experiments to show the effectiveness of the SSL-CC on two benchmark HSIs. We also conduct analysis on the effect of the parameters on the performance of SSL-CC.

A. Dataset

We consider two HSI images: Indian Pines and Pavia University[1]. These images are extensively used within the remote sensing community and Table I summarizes the main characteristics of these images. It is worth noting that the Indian Pines image is acquired over a vegetative area test site in Northwest Indiana, USA. This dataset represents a challenging task since the sixteen land cover types are not balanced and certain classes are represented by a very small number of samples with respect to other classes (20 for Oats vs. 2,455 for Soybean-mintill). Also, this image is taken at the beginning of the growing season, accordingly the captured spectral information are mixed with soil and the previous season crop residue. This attribute adds more complexity to the classification task since most of the classes are from the same category (i.e., crop and vegetable classes). On the other hand, the nine classes on Pavia image are mainly man-made surfaces (Asphalt, Gravel, Painted metal sheets, etc.) which results in a much easier classification task than Indian Pines.

[1]http://www.ehu.eus/ccwintco/index.php?title=Hyperspectral_Remote_Sensing_Scenes

	Indian Pines	Pavia University
Sensor	AVIRIS	ROSIS
Image size	(145 x 145)	(350 x 250)
Ground resolution (m)	20	1.3
# of Bands	200	103
# of Classes	16	9
Class distribution	20/2,455	947/18,649
# of active pixels	10,249	207,400

TABLE I
CHARACTERISTICS OF THE BENCHMARKS.

B. Performance Evaluation

Algorithm performance has been evaluated using a small percentage of available ground-truth labels (1%, 3%, 4%, and 5% are used in this experiment). Furthermore, results for different window sizes ($W = 1, 3, 5, 7$), and different threshold values ($\tau = 0.2, 0.3, 0.4, 0.5$) for FCM were also collected and reported to aid in studying the effect of these parameters on performance. Although any classifier can be used for the classification task, due to its frequent use in remote sensing, the SVM has been selected for the post-clustering classification task. The performance of the algorithm is evaluated against a baseline SVM classifier trained using only the selected subset of the ground-truth (i.e. no pseudo-labels). A one vs. one multi-class SVM (LIBSVM) implemented by Chang et al. [15] has been used for all classification tasks. To ensure the validity of the results, ten realizations are made for each configuration using different randomly selected subset of the ground-truth labels and we report the mean.

C. SSL Results

The average overall accuracy achieved by SSL-CC for Indian Pines and Pavia University benchmarks are presented in Table II and Table III respectively. It is clear from these results that when the number of ground-truth samples is small, SSL-CC improves classification results. The best increase in the classification performance is observed (59.8% improvement) when $\tau = 0.2$ and $W = 5$ with only very small number of ground-truth samples %1 for the Indian Pines benchmark. A similar observation can be made for the Pavia benchmark with the exception that the improvement here is only about 16%. The poor accuracy (49%) using purely supervised learning for the Indian Pines benchmark justifies the use of SSL. On the other hand, purely supervised learning on Pavia was considerably higher (83.4%). Another interesting observation is the fact that the improvements in general decline as τ increases. Since SSL-CC adds pixels that hold higher similarity, as a result, fewer pixels will be added to the training set. Although the performance of SSL-CC based on fuzzy clustering (SSL-CC FCM) is on average better than the k-means based technique (SSL-CC k-means) for small number of ground-truth samples. However, as the number of ground-truth samples increases, SSL-CC k-means performance improves, especially for larger window sizes. Two aspects need to be addressed here: The quality of the generated pseudo-labels and the number of generated pseudo-labels.

W	Training Size	Baseline (SVM)	SSL-CC-FCM (τ) 0.2	0.3	0.4	0.5	SSL-CC k-menas
1	1%	0.490	**0.658**	0.614	0.563	0.525	0.618
3			**0.759**	0.672	0.577	0.529	0.701
5			**0.783**	0.657	0.561	0.525	0.740
7			**0.781**	0.621	0.550	0.523	0.763
1	3%	0.635	**0.766**	0.730	0.692	0.660	0.750
3			**0.839**	0.759	0.687	0.655	0.812
5			**0.839**	0.735	0.673	0.653	0.834
7			0.813	0.702	0.667	0.645	**0.842**
1	4%	0.658	**0.799**	0.758	0.720	0.686	0.781
3			**0.866**	0.787	0.709	0.676	0.842
5			0.859	0.748	0.689	0.672	**0.865**
7			0.825	0.705	0.684	0.668	**0.866**
1	5%	0.688	**0.819**	0.782	0.744	0.711	0.806
3			**0.883**	0.807	0.730	0.701	0.866
5			0.873	0.771	0.714	0.700	**0.883**
7			0.833	0.733	0.710	0.695	**0.886**

TABLE II
INDIAN PINES SSL OVERALL ACCURACY.

W	Training Size	Baseline (SVM)	SSL-CC-FCM (τ) 0.2	0.3	0.4	0.5	SSL-CC k-menas
1	1%	0.834	**0.934**	0.931	0.925	0.914	0.925
3			**0.958**	0.955	0.951	0.937	0.944
5			**0.966**	0.964	0.961	0.944	0.951
7			**0.965**	0.965	0.963	0.944	0.958
1	3%	0.891	**0.950**	0.947	0.942	0.936	0.946
3			**0.971**	0.968	0.963	0.954	0.961
5			**0.977**	0.975	0.971	0.958	0.969
7			**0.974**	**0.974**	0.973	0.959	**0.974**
1	4%	0.919	**0.959**	0.956	0.951	0.945	0.954
3			**0.978**	0.975	0.971	0.962	0.969
5			**0.984**	0.982	0.978	0.966	0.976
7			0.978	0.978	0.976	0.964	**0.980**
1	5%	0.921	**0.960**	0.958	0.954	0.948	0.957
3			**0.981**	0.978	0.974	0.965	0.973
5			**0.985**	0.984	0.980	0.968	0.979
7			0.980	0.980	0.979	0.966	**0.983**

TABLE III
PAVIA UNIVERSITY SSL ACCURACY

1) Quality of pseudo-labels: It is expected that not al generated pseudo-labels are accurate and inaccurate pseudo-labels would affect the final accuracy of the SSL-CC. Fig. 2 shows the accuracy of the generated pseudo-labels for both datasets. The quality is almost perfect when only the direc neighbors are considered; however, as the size of the neighbo window increases, the accuracy of the pseudo-labels decreases for both datasets. The worst accuracy is obtained when $W = 7$ and $\tau = 0.2$. This is expected, since with a smaller threshold value and larger windows it is more likely to generate miss-classified pseudo-labels. On the other hand, the pseudo-labels generated using k-means are almost perfect in all cases because the uncertainty is minimized when crisp clustering is used to generate pseudo-labels.

2) Quantity of pseudo-labels: Fig. 3 shows the number of the pseudo-labels generated for each configuration. For FCM, an almost linear relationship can be observed between the number of ground-truth samples and the number of pseudo-labels especially with small window sizes. It is also observed that the number of pseudo-labels starts to decline with larger threshold values. SSL-CC based on k-means shows similar behavior, however, k-means is able to generate more pseudo-

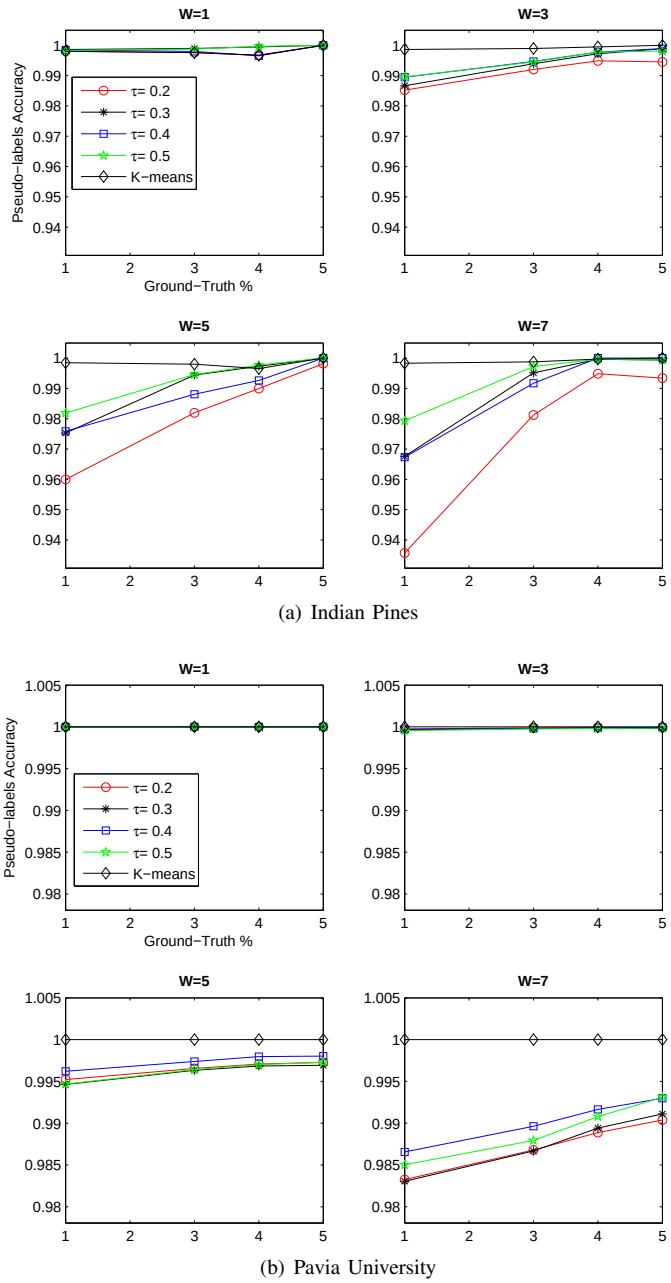

(a) Indian Pines

(b) Pavia University

Fig. 2. Quality of pseudo-labels

labels for small windows and is less sensitive to overlap as disagreement between the pixels will not be as frequent as with FCM.

V. CONCLUSION

In this paper we proposed a semisupervised framework that employs clustering with minimum ground-truth samples to enhance the performance of HSI classification. Results obtained using different datasets confirm that there is a strong correlation between spectral clustering and the image context. The usage of fuzzy membership adds freedom to the degree of similarity between pixels which significantly increases the number of pixels to be added to the ground-truth samples.

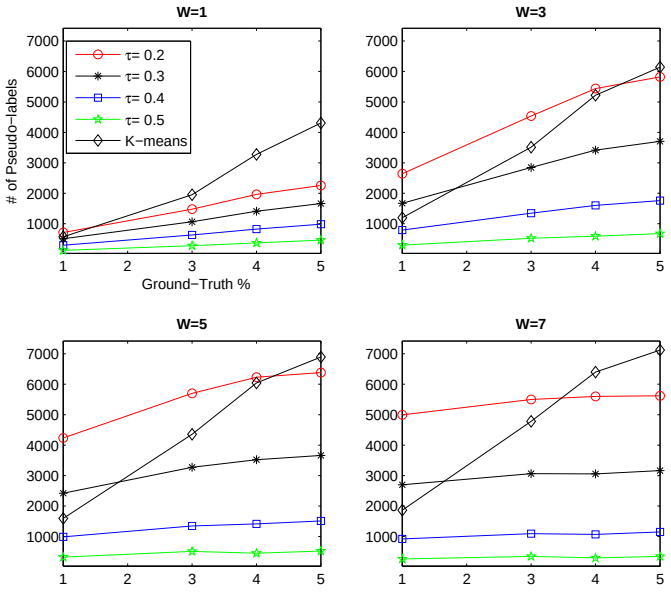

(a) Indian Pines

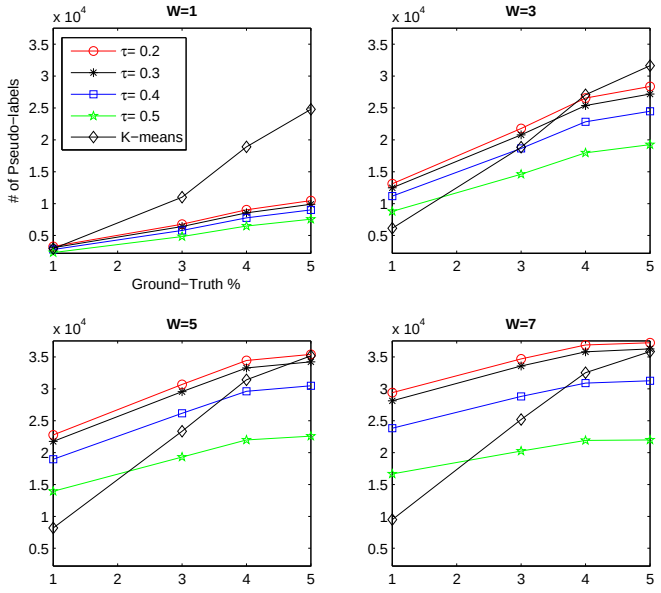

(b) Pavia University

Fig. 3. Quantity of pseudo-labels

However, this relaxation has a price, as some of these pixels will be labeled incorrectly and therefore the classification model will be built with noisy data. Nevertheless, due to the enormous uncertainty in HSI, these incorrectly labeled pixels do not significantly impact the general performance of the complete system. In fact, they act as a regularizer that increases the classifier's ability to generalize. Therefore, FCM is considered as a liberal approach when a small threshold value is used. A notable improvement (59.8%) is obtained in the setting where baseline classification results using only a small set of ground-truth is poor. However, once the number of ground-truth samples exceeds a certain limit, the unsupervised contribution to learning is significantly reduced and may reach a point at which it saturates.

The framework can be successfully applied to very high resolution images acquired by UAS, such that the user is required only to annotate a few pixels and still able to obtain high quality classification maps. In the future, more experiments will be carried out to compare these findings with similar approaches using the same experimental setup. Another interesting future direction is to incorporate fuzzy clustering within an active learning paradigm, where the clustering results would help in finding the most appropriate samples to be annotated by the user. We also will consider employing ensembles of clustering algorithms.

ACKNOWLEDGMENT

The authors would like to thank Prof. D. Landgrebe from Purdue University, USA, and Prof. P. Gamab from University of Pavia, Italy, for providing the hyperspectral images.

REFERENCES

[1] T. Lillesand, R. W. Kiefer, and J. Chipman, *Remote sensing and image interpretation*. John Wiley & Sons, 2014.

[2] G. Camps-Valls, D. Tuia, L. Gómez-Chova, S. Jiménez, and J. Malo, *Remote sensing image processing*. Morgan & Claypool Publishers, 2011.

[3] K. P. Murphy, *Machine learning: a probabilistic perspective*. MIT press, 2012.

[4] J. Bioucas-Dias, A. Plaza, G. Camps-Valls, P. Scheunders, N. Nasrabadi, and J. Chanussot, "Hyperspectral remote sensing data analysis and future challenges," *Geoscience and Remote Sensing Magazine, IEEE*, vol. 1, no. 2, pp. 6–36, 2013.

[5] A. K. Jain, M. N. Murty, and P. J. Flynn, "Data clustering: a review," *ACM computing surveys (CSUR)*, vol. 31, no. 3, pp. 264–323, 1999.

[6] B. M. Shahshahani and D. A. Landgrebe, "The effect of unlabeled samples in reducing the small sample size problem and mitigating the hughes phenomenon," *Geoscience and Remote Sensing, IEEE Transactions on*, vol. 32, no. 5, pp. 1087–1095, 1994.

[7] F. Melgani and L. Bruzzone, "Classification of hyperspectral remote sensing images with support vector machines," *Geoscience and Remote Sensing, IEEE Transactions on*, vol. 42, no. 8, pp. 1778–1790, 2004.

[8] L. Bruzzone, M. Chi, and M. Marconcini, "A novel transductive svm for semisupervised classification of remote-sensing images," *Geoscience and Remote Sensing, IEEE Transactions on*, vol. 44, no. 11, pp. 3363–3373, 2006.

[9] M. Belkin, P. Niyogi, and V. Sindhwani, "Manifold regularization: A geometric framework for learning from labeled and unlabeled examples," *The Journal of Machine Learning Research*, vol. 7, pp. 2399–2434, 2006.

[10] D. Tuia and G. Camps-Valls, "Semisupervised remote sensing image classification with cluster kernels," *Geoscience and Remote Sensing Letters, IEEE*, vol. 6, no. 2, pp. 224–228, 2009.

[11] Y. Tarabalka, J. A. Benediktsson, and J. Chanussot, "Spectral–spatial classification of hyperspectral imagery based on partitional clustering techniques," *IEEE Transactions on Geoscience and Remote Sensing*, vol. 47, no. 8, pp. 2973–2987, 2009.

[12] A. K. Alok, S. Saha, and A. Ekbal, "Pixel classification of remote sensing satellite image using semi-supervised clustering," in *2014 9th International Conference on Industrial and Information Systems (ICIIS)*, pp. 1–6, IEEE, 2014.

[13] J. C. Bezdek, *Pattern recognition with fuzzy objective function algorithms*. Kluwer Academic Publishers, 1981.

[14] P. S. S. Aydav and S. Minz, "Modified self-learning with clustering for the classification of remote sensing images," *Procedia Computer Science*, vol. 58, pp. 97–104, 2015.

[15] C.-C. Chang and C.-J. Lin, "LIBSVM: A library for support vector machines," *ACM Transactions on Intelligent Systems and Technology*, vol. 2, pp. 27:1–27:27, 2011.

Detecting White Mold Onset in Snap Beans Using Spectral Remote Sensing With and Extension to Unmanned Aerial Systems (UAS)

Sadie Wolters, Rochester Institute of Technology, Lindsay Martinescu, Rochester Institute of Technology, Carl Salvaggio, Rochester Institute of Technology, and Jan van Aardt, Rochester Institute of Technology

Precision agriculture with remote sensing from unmanned aerial systems (UAS) is a growing field of research, with applications such as variable rate fertilizer assessment, yield modeling, and mapping of crop disease. White mold, a fungus that impacts snap beans in upstate New York, among other locations, is one example of the latter. Early detection of white mold in snap beans is crucial in limiting the spread and impact of the fungus, since farmers can react in a pro-active manner to address potential yield losses. A variety of fungicide treatments exist to treat or protect crops that are affected by white mold; however, these may also affect the vigor of infected plants. We collected spectral data, using both a handheld spectroradiometer and a Tetracam (6-band multispectral sensor) flown on a DJI octacopter, in an attempt to assess our ability to detect the onset of white mold over the course of a growing season. As the field of UAS research grows, and the cost of equipment decreases, more applications for UAS are being developed, which can allow practitioners, such as farmers, to solve real world problems. Various established approaches to spectral analysis, such as logistic regression, normalized difference vegetation indices, and established vegetation indices will be used to assess plant vigor over time as a function of different fungicide treatments. Data were collected at a controlled/research snap bean field(Geneva, NY, USA; Cornell Plant Pathology and Plant-Microbe Biology Section). This field had controlled watering, fertilization, and inoculation of white mold, as well as various fungicide treatments. The multispectral imagery was acquired with the Tetracam at multiple stages throughout the season, while the handheld spectroradiometer data were collected for approximately 10 days following white mold inoculation. The ability to assess disease onset and plant health using such methods could aid farmers in the economical and sustainable management of their crops via judicial fungicide usage. Initial results related to disease detection and treatment efficacy will be presented at the conference.

On Mapping Corn Yield Using Structure-from-motion Data from Unmanned Aerial Systems (UAS)

Seth Baker, Rochester Institute of Technology, Jan van Aardt, Rochester Institute of Technology, and Carl Salvaggio, Rochester Institute of Technology,

Modern agriculture requires effective application of chemicals, such as fertilizer and pesticides, in order to meet the yield demands of the world's growing population. However, while existing approaches generally are effective, they are far from efficient and can result in negative impacts on the environment and are not cost-optimized. For these reasons, precision agriculture, as well as the push for the development of a carbon credit market, have grown in popularity to increase yield and chemical application efficiency, while minimizing environmental impacts. Unmanned aerial systems (UAS) can provide imagery for a rapid, cost-effective solution to address these three elements. Structure-from-motion techniques, as well as various image interpolation and 3D volume estimations, can be utilized to produce a 3D model of crops from this imagery, effectively enabling the mapping of vegetation structure within a field. This paper will assess the accuracy of 3D crop models of a corn field (Lyons, NY, USA) at different stages during the growing season, with the eventual goal of using 3D structural metrics as independent variables to develop corn yield and biomass (carbon) models. Ground truth measurements from harvest (October 2016) will provide data for accuracy assessment of relevant 3D structure, as well as yield and biomass estimates. Accurate and precise yield estimates would provide farmers with pro-active information related to field locations where spatially-explicit fertilization may improve eventual yield, as well as aid with inventory of total corn biomass, i.e., potential carbon credits. Initial 3D structure assessment results will be presented at the symposium.

Notes: